

ATOMS: ALMA Three-millimeter Observations of Massive Star-forming regions - III. Catalogues of candidate hot molecular cores and Hyper/Ultra compact HII regions

Hong-Li Liu,^{*1,4,2} Tie Liu,^{*2,3} Neal J. Evans,^{5,6} Ke Wang,⁷ Guido Garay,⁸ Sheng-Li Qin,¹ Shanghuo Li,⁶ Amelia Stutz,^{4,9} Paul F. Goldsmith,¹⁰ Sheng-Yuan Liu,¹¹ Anandmayee Tej,¹² Qizhou Zhang,¹³ Mika Juvela,¹⁴ Di Li,^{15,16,17} Jun-Zhi Wang,^{2,18} Leonardo Bronfman,⁸ Zhiyuan Ren,¹⁵ Yue-Fang Wu,¹⁹ Kee-Tae Kim,^{6,20} Chang-Won Lee,^{6,20} Ken'ichi Tatematsu,²¹ Maria. R. Cunningham,²² Xun-Chuan Liu,¹⁹ Jing-Wen Wu,¹⁵ Tomoya Hirota,²¹ Jeong-Eun Lee,²³ Pak-Shing Li,²⁴ Sung-Ju Kang,⁶ Diego Mardones,⁸ Isabelle Ristorcelli,²⁵ Yong Zhang,²⁶ Qiu-Yi Luo,² L. Viktor Toth,²⁷ Hee-weon Yi,²³ Hyeong-Sik Yun,²³ Ya-Ping Peng,²⁸ Juan Li,^{2,18} Feng-Yao Zhu,² Zhi-Qiang Shen,^{2,18} Tapas Baug,^{7,29} Lokesh Dewangan,³⁰ Eswaraiah Chakali,¹⁵ Rong Liu,¹⁵ Feng-Wei Xu,¹⁹ Yu Wang,¹⁹ Chao Zhang,^{31,15} Jinzeng Li,¹⁵ Chao Zhang,¹ Jianwen Zhou,¹⁵ Mengyao Tang,¹ Qiaowei Xue,¹ Namitha Issac,¹² Archana Soam,³² Rodrigo H. Álvarez-Gutiérrez⁴

Affiliations are listed at the end of the paper

Accepted 7 May 2021; Received 7 May; in original 22 December 2020

ABSTRACT

We have identified 453 compact dense cores in 3 mm continuum emission maps in the ATOMS (ALMA Three-millimeter Observations of Massive Star-forming regions) survey, and compiled three catalogues of high-mass star forming cores. One catalogue, referred to as H/UC-HII catalogue, includes 89 cores that enshroud hyper/ultra compact (H/UC) HII regions as characterized by associated compact H40_α emission. A second catalogue, referred to as pure s-CHMC, includes 32 candidate Hot Molecular Cores (HMCs) showing rich spectra ($N \geq 20$ lines) of complex organic molecules (COMs) but not associated with H/UC-HII regions. The third catalogue, referred to as pure w-CHMC, includes 58 candidate HMCs with relatively low levels of COM richness and not associated with H/UC-HII regions. These three catalogues of dense cores provide an important foundation for future studies of the early stages of high-mass star formation across the Milky Way. We also find that nearly half of H/UC-HII cores are candidate HMCs. From the number counts of COM-containing and H/UC-HII cores, we suggest that the duration of high-mass protostellar cores showing chemically rich features is at least comparable to the lifetime of H/UC-HII regions. For cores in the H/UC-HII catalogue, the width of the H40_α line increases as the core size decreases, suggesting that the non-thermal dynamical and/or pressure line-broadening mechanisms dominate on the smaller scales of the H/UC-HII cores.

Key words: stars: formation - stars: kinematics and dynamics; ISM: HII regions; ISM: clouds.

1 INTRODUCTION

High-mass stars ($M_* > 8 M_\odot$) play a crucial role in many astrophysical processes, for example from the formation of solid material in the early Universe (Dunne et al. 2003) to the influence on the evolution of their host galaxies and future generations of star formation in their natal molecular clouds (e.g., Kennicutt 2005; Urquhart et al. 2014). Despite its importance on different (time and spatial) scales, high-mass star formation remains much less understood than low-mass star formation due to the observational challenges presented

by increased distances, rarity, opaque surroundings, and short formation timescales (e.g., Zinnecker & Yorke 2007; Tan et al. 2014; Motte, Bontemps, & Louvet 2018). In addition, high-mass protostars are embedded in a rich cluster environment (e.g., de Wit et al. 2005), which makes it very difficult to disentangle the physical formation processes of high-mass stars and numerous low-mass cluster members

Despite the observational difficulties mentioned above, it has been known for the past 15 years that high-mass stars spend a considerable fraction of their lifetime ($> 10\%$) embedded in their natal molecular clouds (e.g., van der Tak 2004). From an observational perspective, this embedded phase can be generally subdivided into

* E-mail: honglilui2012@gmail.com, and liutie@shao.ac.cn

four different groups of objects that represent different evolutionary stages. **1)** Massive dense cores (MDCs, $M \gtrsim 30 M_{\odot}$ within ~ 0.1 pc). They are generally the nurseries of high-mass star formation (e.g., Zhang et al. 2009; Wang et al. 2011; Zhang et al. 2015; Motte, Bontemps, & Louvet 2018; Sanhueza et al. 2019; Li et al. 2019; Svoboda et al. 2019), and perhaps analogous to the prestellar cores in low-mass star formation regions if they are completely starless. **2)** High-mass protostellar objects (HMPOs). They are very luminous, with bolometric luminosities above $10^3 L_{\odot}$, and deeply embedded within massive envelopes having centrally-peaked temperature and density distributions. At this stage, a (pseudo) disk is formed to transfer onto the HMPOs the infalling material from the envelope (e.g., Beuther et al. 2002; McKee & Tan 2003; Cesaroni et al. 2007). **3)** Hot molecular cores (HMCs). They correspond to the compact (< 0.1 pc), dense ($\geq 10^5 - 10^8 \text{ cm}^{-3}$), massive ($\sim 100 M_{\odot}$), and hot ($\gtrsim 100$ K) molecular material that is radiatively heated intensively (e.g., Kurtz et al. 2000; Rathborne et al. 2011; Hosokawa & Omukai 2009). Consequently, the intense radiative heating enriches the gas phase with many complex organic molecules (COMs) such as CH_3OCH_3 and CH_3OCHO . **4)** Hyper/ultra compact (H/UC)-HII regions. The UC-HII regions refer to those with sizes ≤ 0.1 pc, densities $> 10^4 \text{ cm}^{-3}$, and emission measures $\geq 10^7 \text{ pc cm}^{-6}$ (e.g., Wood & Churchwell 1989; Hoare et al. 2007). The HC-HII regions, which are a newly identified class of compact HII regions after the discovery of UC-HII, correspond to those with sizes ≤ 0.05 pc, densities $> 10^6 \text{ cm}^{-3}$, and emission measures $\geq 10^7 \text{ pc cm}^{-6}$ (Kurtz & Hofner 2005; Hoare et al. 2007; Yang et al. 2019, 2020).

During the past decades, studies of the embedded phase of high-mass star formation have made much progress. After a large number of IRDCs were revealed by Infrared Space Observatory (ISO, Perault et al. 1996), Midcourse Space Experiment (MSX, Egan et al. 1998), and *Spitzer* (Peretto & Fuller 2009), several surveys in (sub)millimeter continuum and spectral lines followed (e.g., Rathborne, Jackson, & Simon 2006; Ragan et al. 2006; Simon et al. 2006; Rathborne et al. 2010; Dirienzo et al. 2015; Sanhueza et al. 2019), and have established that massive IRDCs harbor the early, embedded stages of high-mass star and cluster formation. In particular, the recent ALMA 1 mm survey ASHES led by Sanhueza et al. (2019), which was designed to mosaic 12 massive ($> 500 M_{\odot}$), cold (≤ 15 K), 3.6–70 μm dark-cloud clump at the resolution ~ 4000 AU and mass sensitivity better than $0.2 M_{\odot}$, revealed a large population of low-mass ($< 1 M_{\odot}$) cores but no high-mass ($> 30 M_{\odot}$) prestellar cores on the 0.01–0.1 pc scales. With detailed analysis, the authors also put several strong observational constraints on cloud fragmentation, the clustering mode of dense cores, and the dynamical collapse scenario at the early stages of high-mass star formation.

As for the HMPO and HMC stages, both have many observational similarities except for the abundance of COMs; for example, they both are accompanied by massive molecular outflows, infall and even rotation (e.g., Zhang et al. 2001, 2005; Beuther et al. 2002; van der Tak 2004; Liu et al. 2017). Some important physical processes including mass accretion and disk rotation related to the HMPOs can therefore be understood from the investigation into the HMCs since the latter is generally accompanied by rich molecular line emission that bears both physical and chemical imprints of high-mass star formation (e.g., Keto & Zhang 2010; Qiu et al. 2012). Focusing on the HMCs, we find that most of the efforts so far have been toward individual sources or small samples through single-dish and/or interferometric observations in the (sub)millimeter regime (e.g., van der Tak 2004; Beuther 2007; Qin et al. 2008; Purcell et al. 2009; Cesaroni et al. 2010; Furuya, Cesaroni, & Shinnaga 2011; Rathborne

et al. 2011; Xu & Wang 2013; Hernández-Hernández et al. 2014; Qin et al. 2015; Silva et al. 2017; Csengeri et al. 2019; Coletta et al. 2020; Belloche et al. 2020; Sato et al. 2020). Although these studies have demonstrated the HMC as an ideal laboratory in which to search for infall, outflow, and rotation motions related to high-mass star formation, these important physical processes are still far from being well understood mainly due to the lack of deep, interferometric (sub)millimetre observations toward a sufficiently large sample of HMCs. For the H/UC-HII stage, the situation improves; there are several surveys that serve to characterize the H/UC-HII regions, such as IRAS warm dust continuum at far-IR wavelengths (Wood & Churchwell 1989; Kurtz, Churchwell, & Wood 1994), CORNISH 5 GHz radio continuum (Hoare et al. 2012; Purcell et al. 2013), and ATLASGAL 870 μm cold dust continuum (Schuller et al. 2009; Urquhart et al. 2013) surveys. These surveys help define observationally the H/UC-HII regions reasonably well in terms of their sizes, densities, and emission measures (see above).

In addition, some H/UC-HII regions are likely still accreting mass, despite the high pressure of ionized gas (e.g., Sollins et al. 2005; Keto 2007; Keto, Zhang, & Kurtz 2008). However, the role that H/UC-HII regions play in the early stages of high-mass star formation remains to be understood. Hopefully, the H/UC-HII regions can light up their immediate surroundings and allow the investigation of the properties (e.g., density distribution, and velocity field) of the surrounding region in which high-mass stars are formed (e.g., Hoare et al. 2007). The immediate vicinities of H/UC-HII regions have been the subject of the (sub)millimeter observation studies, however, the lack of high-angular resolution observations has impeded anything like complete understanding of H/UC-HII region physics.

In this paper, the third in a series from ATOMS¹ (e.g., Liu et al. 2020a, Liu et al. 2020b, hereafter, Paper I and Paper II, respectively), we take advantage of deep, high-resolution ALMA 3 mm observations (see below) of the ATOMS survey. In Paper I, we introduced the main scientific goals of the survey through a case study for the G9.62+0.19 complex, including to systematically investigate the spatial distribution of various dense gas tracers in a large sample of Galactic massive star-forming clumps, to study the roles of stellar feedback in star formation, and to characterize filamentary structures inside massive clumps. In paper II, we studied the star formation scaling relations inferred from different dense gas tracers, and suggested that both the main and isotopologue lines (i.e., $\text{HCO}^+/\text{H}^{13}\text{CO}^+$, $\text{HCN}/\text{H}^{13}\text{CN}$) are good tracers of the total mass of dense gas in Galactic molecular clumps, and that the large optical depths of the main lines do not affect the interpretation of the slopes in star formation relations.

With the ATOMS survey data, in this paper we aim to establish catalogues of a large sample of both candidate HMCs and H/UC-HII regions as a crucial foundation for future studies for the early stages of high-mass star formation. The ATOMS survey targeted a large sample of 146 IRAS clumps (Bronfman, Nyman, & May 1996; Liu et al. 2016), which have masses 5.6 to $2.5 \times 10^5 M_{\odot}$ with a median value of $1.4 \times 10^3 M_{\odot}$, radii 0.06 to 4.26 pc with a median value of 0.86 pc, and bolometric luminosities 16 to $8.1 \times 10^6 L_{\odot}$ with a median value of $5.7 \times 10^4 L_{\odot}$ (see Table A1 of Paper I). All the targets except for I080763556 and I115906452 have bolometric luminosities greater than $10^3 L_{\odot}$, and actually more than 90% of them are high-mass star-forming regions (see Paper I, and Paper II). In addition, the ATOMS targets are located in the first and fourth Galactic

¹ ATOMS: ALMA Three-millimeter Observations of Massive Star-forming regions survey

Quadrants of the inner Galactic plane ($-80^\circ < l < 40^\circ$, $|b| < 2^\circ$) at distances 0.4 to 13.0 kpc (the corresponding Galactocentric distances 0.5 to 12.7 kpc, see Appendix A for the distance calculations). Twenty-seven distant ($d \geq 7$ kpc) sources are either close to the Galactic Centre or mini-starbursts (like W49N/I19078+0901), representing extreme environments for star formation. Overall, the ATOMS survey contains a diversity of objects suitable for studying the early stages of high-mass star formation, especially HMC and H/UC-HII stages, with different physical conditions – including densities and luminosities – and in different environments, across a large range of Galactocentric distances.

This paper is organized as follows: Section 2 gives a brief description about the ALMA observations of the ATOMS survey, Section 3 presents the results of the extraction and search of the candidate HMC and H/UC-HII cores, Section 4 presents a discussion, and Section 5 includes the conclusions and a summary of our results.

2 ALMA OBSERVATIONS

We make use of the ATOMS survey data (Project ID: 2019.1.00685.S; PI: Tie Liu, see Paper I and Paper II). The observations were conducted towards the 146 IRAS clumps in the single-pointing mode with both the Atacama Compact 7-m Array (ACA; Morita Array) and the 12-m array (C43-2 or C43-3 configurations) in band 3. Eight spectral windows (SPWs) were tuned to cover 11 commonly-used lines including the dense gas tracers (e.g., HCO^+ , HCN, and their isotopes), HMC tracers (e.g., CH_3OH , and HC_3N), shock tracers (e.g., SiO, and SO), and ionized gas tracers ($\text{H}_{40\alpha}$). The basic parameters (e.g., rest frequency, transition, critical density, and upper energy temperature) of these lines can be found in Table 2 of Paper I. The SPWs 1–6² at the lower side band, with spectral resolutions of $\sim 0.2 - 0.4 \text{ km s}^{-1}$ were chosen to resolve the line profiles in order to investigate the kinematics within high-mass star forming clumps, while the SPWs 7–8 at the upper side band, each with a broad bandwidth of 1875 MHz at a spectral resolution of $\sim 1.6 \text{ km s}^{-1}$, were chosen for continuum emission and line scan observations. Note that the original spectral resolution of the SPWs 7–8 is $\sim 1.6 \text{ km s}^{-1}$ instead of $\sim 3 \text{ km s}^{-1}$ as given in Paper I.

The ACA and 12-m-array data were calibrated and imaged separately with the CASA software package version 5.6 (McMullin et al. 2007), where the continuum image centred at $\sim 93.8 \text{ GHz}$ was cleaned in an aggregated $\sim 4 \text{ GHz}$ frequency bandwidth free of the line-emission. More details on the data reduction can be found in Paper I and Paper II. As we focus in this work on the very dense, compact HMCs and H/UC-HII regions, in what follows we will only consider the 12-m-array data and the analysis is focused on the primary-beam corrected data. The reduced 12-m-array continuum image and line cubes for the 146 target clumps have angular resolutions of $\sim 1''.2 - 1''.9$ (for reference, $2''$ corresponds to 0.1 pc at a distance of 10 kpc), and maximum recoverable angular scales $\sim 14''.5 - 20''.3$. The sensitivity of the 12-m-array data is better than 10 mJy beam^{-1} per 0.122 MHz channel (see Table 1 of Paper I) for lines, and $\sim 0.4 \text{ mJy beam}^{-1}$ for continuum.

² The frequency ranges of the eight spectral windows (SPWs) are [86.311, 86.369] GHz for SPW 1, [86.725, 86.784] GHz for SPW 2, [86.818, 86.876] GHz for SPW 3, [87.288, 87.346] GHz for SPW 4, [88.603, 88.661] GHz for SPW 5, [89.159, 89.218] GHz for SPW 6, [97.530, 99.404] GHz for SPW 7, [99.468, 101.341] GHz for SPW 8.

3 ANALYSIS AND RESULTS

3.1 Core extraction

To extract compact cores from the 3 mm continuum maps, we make use of both the *Dendrogram* algorithm³ and CASA-*imfit* function. *Dendrogram* can be easily used to extract the dense leaf-like structures (hereafter referred to as cores), which are the smallest structures without substructures in the terminology of the algorithm, and thus customarily taken to be the candidates for cores. This technique does not always provide good measurements of the core parameters such as size and position angle, while CASA-*imfit* performs better in this regard through a two-dimensional Gaussian fit to the emission. A visual inspection of the continuum images of the 146 target sources, shows that their outer parts, i.e., the area beyond a radius of 0.01° from the image center, are much noisier than the inner parts, where the 0.01° radius corresponds to the $\text{pblimit} = 0.4$. Therefore, we masked out the outer part of the images before identifying the core structures. To identify cores we followed two steps. First, using *Dendrogram* we find cores and determine their parameters (i.e., centre position, peak flux density, minor and major-axis sizes, and position angle), toward each target clump. Then we made a more accurate measurement of the core parameters using the CASA task *imfit* adopting as initial guesses the parameters determined in the previous step. This approach has been employed in Li et al. (2020), and demonstrated to work very well.

In the first step, as inputs of the three key parameters to the *Dendrogram* algorithm we used: (i) $\text{min_value} = 2\sigma_{3\text{mm}}$, where $\sigma_{3\text{mm}}$ is the noise level. In practice, we first run the *Dendrogram* algorithm to identify the compact cores in the 3 mm continuum image, then subtract them to obtain a nearly-flat residual 3 mm image, and finally estimate the rms level of the residual image as the noise ($\sigma_{3\text{mm}}$) of the original 3 mm continuum image as the starting level to construct the dendrogram. In addition, we used (ii) $\text{min_delta} = \sigma_{3\text{mm}}$, the default value in the algorithm to recognise an independent leaf (i.e., the core structure); and (iii) $\text{min_npix} = N$ pixels, where N was chosen to be equivalent to the area of one beam (depending on the pixel and beam sizes of the image of each target clump). This was imposed to ensure a core to be resolvable. Given the above three parameters, the *Dendrogram* algorithm automatically locates the cores, and measures their parameters (see above). To avoid spurious cores, we performed a post-selection to require the selected cores must have peak flux greater than $5\sigma_{3\text{mm}}$.

In the second step, we used the parameters of the post-selected cores determined in the first step as inputs to run the CASA-*imfit* task to accurately identify the cores, and measure their parameters, including peak position, major and minor sizes (FWHM_{maj} , FWHM_{min}), position angle (PA), peak flux ($F_{3\text{mm}}^{\text{p}}$), and integrated flux ($F_{3\text{mm}}^{\text{int}}$). The measurement uncertainties on the flux are given by CASA-*imfit*. The uncertainties related to the missing flux effect are not taken into account in this work since it is found not significant for compact cores by comparing the 12M data with the combined 12M+7M data (Paper I). Through careful visual inspection of the 3 mm continuum map overlaid with the identified cores, we removed a few fake cores with poorly-fitted shapes. Such cores tend to have a large aspect ratio (> 3) between the major and minor-axis sizes, appearing either as a filamentary structure or as a diffuse emission feature. As a result, we finally obtained 453 cores from the 146 ATOMS target clumps.

The entire extraction procedure is illustrated in Fig. 1, where we

³ <https://dendrograms.readthedocs.io/en/stable/>

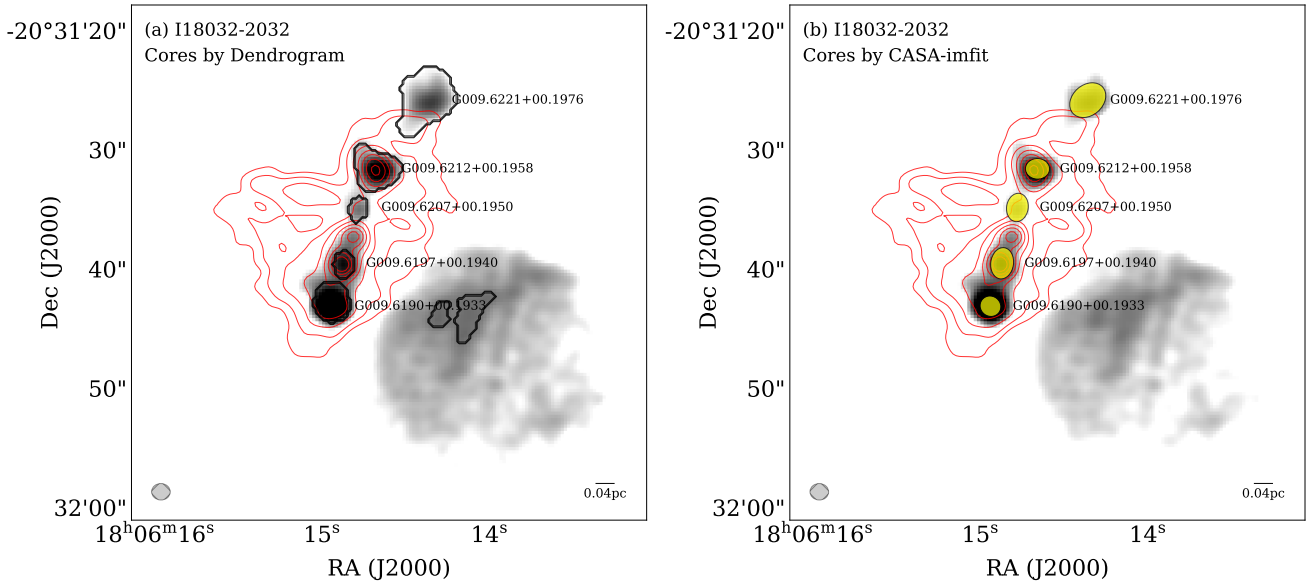


Figure 1. Illustration of the core extraction. (a): the preliminary extraction of seven core structures (in black contour) in the target clump I18032-2302 from 3 mm continuum emission by *Dendrogram*. (b): the final extraction of five finer cores (in yellow ellipses) by *CASA-imfit*. In both panels, 3 mm continuum (in grayscale) is overlaid with the velocity-integrated intensity of HC_3N (in red contours) over $[-35, 45] \text{ km s}^{-1}$. The cores labelled with *Galactic* names are the cores remaining after post-selection (see text). One core, between G009.6197+00.1940 and G009.6207+00.1950, is missing in the second extraction procedure due to either insufficient angular resolution or low contrast against its background. Note that the contour levels start at 3 rms with the steps set by a dynamically determined power-law of the form $D = 3 \times N^p + 2$, where D is the dynamic range of the intensity map (i.e., the ratio between the peak and the rms noise), N is the number of the contours used (8 in this case), and p the contour power-law index. The beam of the 3 mm continuum map and a scale bar of 0.04 pc are indicated at the bottom left, and bottom right of each panel, respectively.

take the target clump I18032-2302 as an example of identifying the cores that are contained. The procedure starts from the compact core extraction on the 3 mm continuum map with *Dendrogram* in the left panel, and then moves to the finer core fitting with *CASA-imfit* in the right panel. Due to the marginal angular resolution ($\sim 2''$) and small intensity contrast in the 3 mm continuum emission maps, some cores may be missed in the core extraction. For example, comparing with the higher intensity-contrast range HC_3N (11-10) emission map, one can see that one molecular core between G009.6197+00.1940 and G009.6207+00.1950 revealed by HC_3N (11-10) is missing in the core extraction procedure. This is because that core cannot be separated from its adjacent cores or background emission in the 3 mm continuum emission map but emerges in higher intensity-contrast HC_3N (11-10) emission map. This issue very rarely occurs in the full sample and predominantly affects low flux (so presumably low-mass) core (specifically, those in the “unknown core” category that contains the cores with unknown nature of star formation so far, see Sect. 3.3). Hence, the analysis in what follows is largely unaffected by this issue.

In addition, with both *Dendrogram* and *CASA-imfit* used in the core extraction, several major parameters measured from both methods can be compared. Actually, we find that the flux and position measurements are consistent in both methods. However, the size measured by *CASA-imfit* is larger than that in *Dendrogram* mainly for the low-flux cores (i.e., in the “unknown cores” category, see Sect. 3.3). The position angle measurement in *CASA-imfit* generally matches the 3 mm continuum dense structure orientation better than that in *Dendrogram*. These differences mainly come from the different methods of parameter determination used in *Dendrogram* and *CASA-imfit*. In the former the size and position angle parameters are derived from the intensity-weighted second moments along the two spatial dimensions (Rosolowsky et al. 2008) while in the

latter the two parameters are directly derived from Gaussian fitting to the unweighted intensity spatial distribution. Therefore, to better reflect the core geometry as seen in 3 mm continuum, we prefer to use the core parameters measured by *CASA-imfit*.

3.2 Search for candidate HMCs and H/UC-HII cores

One important step towards understanding high-mass star formation is to search for the massive cores that harbor the early stages of high-mass star and cluster formation. Clues to high-mass star formation can be inferred from the properties of massive starless and/or prestellar cores (e.g., Yuan et al. 2017), the SED of high-mass protostellar objects (HMPOs, e.g., Rathborne et al. 2005), HMCs (e.g., Kurtz et al. 2000; Rathborne et al. 2011), H/UC-HII regions (e.g., Churchwell 2002; Hoare et al. 2007), and some masers (e.g., Class II CH_3OH masers), which exclusively trace high-mass star formation (e.g., Wang et al. 2014). Here, we focus on the search of massive cores associated with HMCs and H/UC-HII regions. The advantage of the ATOMS survey strategy is that the two wide SPWs 7–8 cover many transitions of the COMs (i.e., HMC tracers; see Fig. 12 of Paper I) and the $\text{H}40_\alpha$ transition (i.e., the ionized gas tracer). In what follows, we discuss the search for H/UC-HII cores in Sect. 3.2.1 and COM-containing cores in Sect. 3.2.2 that could correspond to candidate HMCs.

3.2.1 Search for H/UC-HII Cores

The entire procedure of the H/UC-HII core search is illustrated in Fig. 2, where the core G009.6190+00.1933 from the clump I18032-2302 is taken as an example. In Fig. 2a, the velocity-integrated intensity of $\text{H}40_\alpha$ emission over a velocity range of 150 km s^{-1} centered

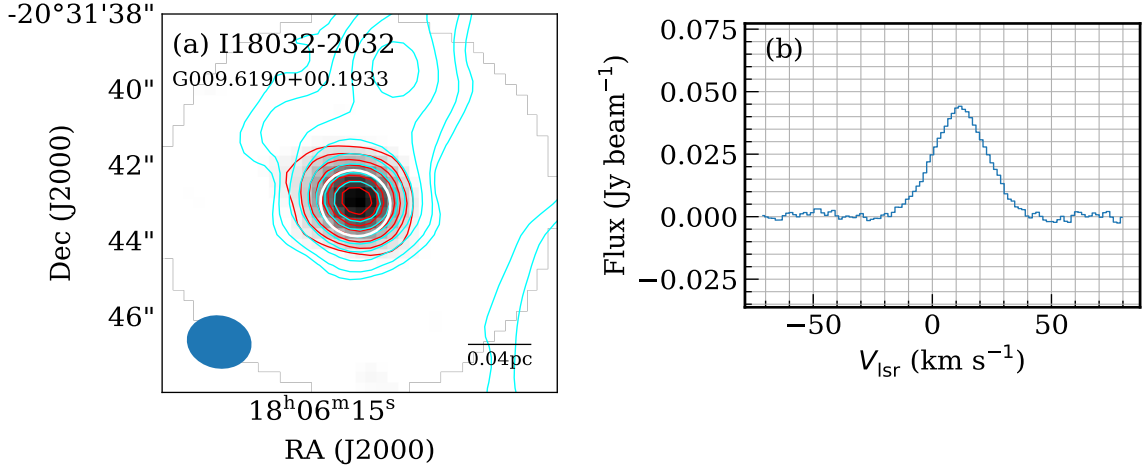


Figure 2. Illustration of the H/UC-HII core search. (a): velocity-integrated intensity map of H40_α (in both grayscale and red contours) over $[-70, 80] \text{ km s}^{-1}$ for the core G009.6190+00.1933 (in white ellipse) in the target clump I18032-2032. The map is centered at the core peak with a size of $10''$. For comparison, the 3 mm continuum is also superimposed in cyan contours. The synthesized beam and a scale bar of 0.04 pc are drawn at the bottom of the panel. (b): beam ($2''$)-averaged spectrum of H40_α at the core centre. G009.6190+00.1933 is an H/UC-HII core as characterized by strong, and compact H40_α emission.

at the systemic velocity of the core (in both the grayscale and red contours) is overlaid with the 3 mm continuum (cyan contours). The core in question is indicated by the white ellipse. Figure 2b presents the beam-averaged spectrum of H40_α at the core center. If the H40_α emission appears compact and is spatially associated with the compact continuum core, the core will be classified as an H/UC-HII core. Following this rule, we finally obtain 89 H/UC-HII cores. Their parameters determined by CASA-*imfit* are given in Table 1, including the clump and core names (i.e., Cols. 1–2), the measured sizes of the major and minor axes and the position angle (i.e., Cols. 4–5), the deconvolved sizes of both axes (i.e., Cols. 6), the core-integrated 3 mm flux (i.e., Col. 7), the core-peak flux (i.e., Col. 8). The radii (i.e., Col. 9) of the cores were calculated assuming the same distance as that of their natal clumps (see Paper I). In addition, we measured the line peak intensity ($F_{\text{H40}_\alpha}^{\text{p}}$), the velocity centroid ($V_{\text{lsr}, \text{H40}_\alpha}$), the line width ($\Delta V_{\text{H40}_\alpha}$) of the H40_α line for each H/UC-HII core by fitting a single-Gaussian component to the beam-averaged spectrum of H40_α . For comparison (see Sect. 4.5), the deconvolved size of the H/UC-HII cores from H40_α emission was also measured with CASA-*imfit* and the corresponding radius ($\Delta R_{\text{core}}^{\text{H40}_\alpha}$) was computed as above. These parameters can also be found in last five columns of Table 1. The $\Delta R_{\text{core}}^{\text{H40}_\alpha}$ and $\Delta V_{\text{H40}_\alpha}$ together suggest that the cores with associated compact H40_α emission are indeed H/UC-HII sources (see Sect. 4.5).

3.2.2 Search for COM-containing cores

To quantitatively describe the chemical richness of a core, we use the number of lines (N_{line}) detected in the two line-scan windows SPWs 7–8. These spectral windows cover tens of transitions from COMs (e.g., CH_3OCHO , CH_3CHO , CH_3OH , $\text{C}_2\text{H}_5\text{CN}$) that are usually detectable in a HMC, and only two or three transitions of non HMC-tracer molecules (i.e., CS (2–1), SO (3–2) or H_2CO , see Fig. 12 of Paper I). Counting the emission lines is therefore useful in a search for the COM-containing cores.

The number of emission lines was determined by searching for emission peaks above the 3σ level across the entire spectrum of the two SPWs, which was also adopted in Sánchez-Monge et al. (2017). In practice, the 1σ level was calculated individually for each

source from the standard deviation of the amplitudes in the line-free emission channels usually located on either or both ends of the wide SPWs. This method works very well for the sources without a forest of detectable lines. However, it is generally conservative for the sources (e.g., the one in Fig. 3a) with a forest of detectable lines since it is difficult to find completely line-free channels, leading to an overestimate of the sigma level. To avoid counting spurious peaks, for example from the broad line wings of the spectrum of the outflow sources, the separation between the nearest neighbours was required to be at least five velocity channels (i.e., $\sim 8 \text{ km s}^{-1}$). In addition, a valid peak detection was required to have at least three channels above the 3σ level.

Figure 3 displays an example of the search for the emission lines from the beam-averaged spectrum of the two SPWs at the peak position of two cores, demonstrating that our method works well in counting emission lines. Note that the two sources given in the example were in different ALMA observing clusters with the center frequencies slightly different, so that the frequency ranges of the sources are different accordingly. The final COM-containing cores are defined by the following two criteria, $N_{\text{line}} \geq 5$ and a compact feature of HC_3N emission. The former ensures at least one transition of the COMs for each candidate (see above, and Fig. 3), while the latter requires each candidate to be a compact source in molecular line emission. Figure 4 presents an example of the compact COM-containing core in HC_3N emission. Figure 4a shows the velocity-integrated intensity of HC_3N (in both grayscale and red contours) over a velocity extent of 80 km s^{-1} centered at the systemic velocity of the core (in white ellipse) and 3 mm continuum (in cyan contours), while Fig. 4b displays the beam-averaged spectrum of HC_3N at the core center.

Following the above two criteria, 138 COM-containing cores were selected. We find that 48 out of these 138 COM-containing cores are spatially associated with H/UC-HII cores (positions matching within a radius of $2''$, comparable to the beam size), and thus are H/UC-HII-associated candidate HMCs (cHMCs, hereafter). Note that the HMC is a definition from the molecular chemistry study, and has been observationally found to overlap the H/UC-HII regions. Given their masses and densities (see Sect. 4.2) most of the

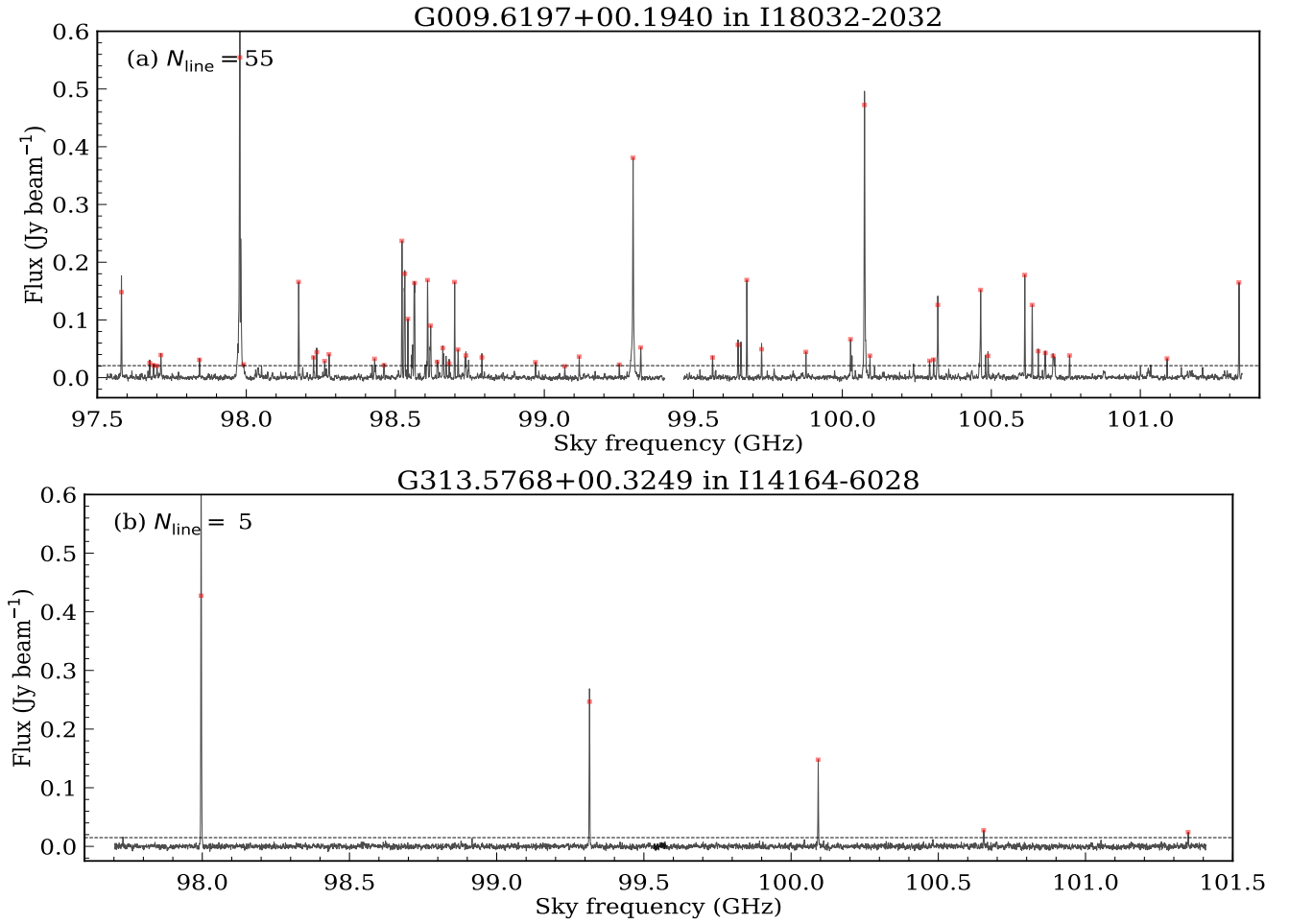


Figure 3. Beam (2'')-averaged spectrum of SPWs 7–8 at the emission peak of the two COM-containing cores (see definition in text) from two ATOMS clumps. The core and clump names are labelled on top of each panel. The red squares indicate the emission lines above 3 rms and their total number is given to the parameter N_{line} . The horizontal dashed line indicates the 3 rms noise level across the two spectral windows. For reference, the five lines of panel b in an order of decreasing intensity are CS (2-1), SO (3-2), HC₃N (11-10), CH₃OH and H₂CO, respectively.

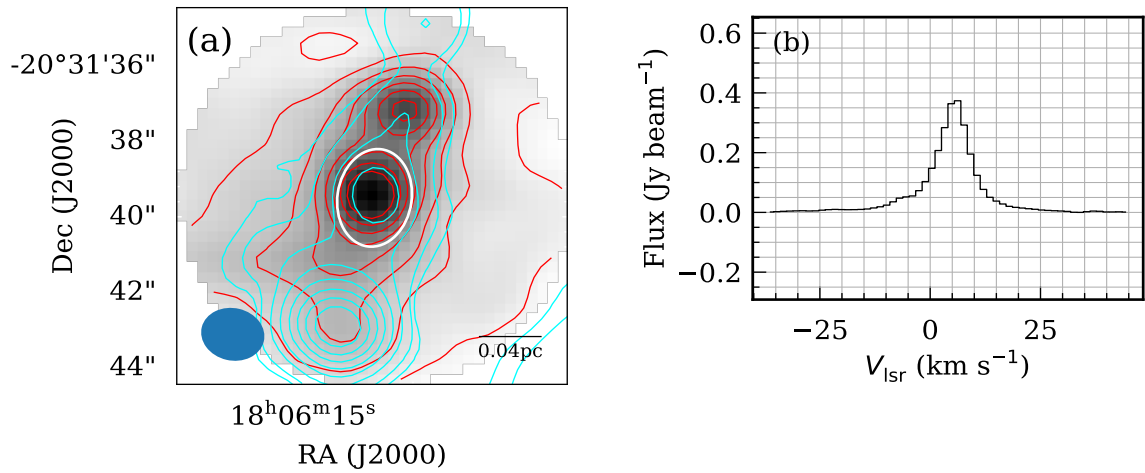


Figure 4. (a): velocity-integrated intensity map of HC₃N over $[-35, 45] \text{ km s}^{-1}$ (in both grayscale and red contours) for the G009.6197+00.1940 core (in white ellipse) and its surroundings. The map is centred at the core peak with a size of 10''. For comparison, the 3 mm continuum is superimposed in cyan contours. The synthesized beam and a scale bar of 0.04 pc are drawn at the bottom left of the panel. (b): beam (2'')-averaged spectrum of HC₃N at the core centre (i.e., the white ellipse in panel a).

Table 1. Parameters of the H/UC-HII cores from the ATOMS survey's clumps.

Name Clump	Gal. Name core	D kpc	$FWHM$ maj(") \times min(")	PA deg	$FWHM_{dec}$ maj(") \times min(")	F_{3mm}^{int} mJy	F_{3mm}^p mJy beam $^{-1}$	R_{core} 10^{-2} pc	$F_{H40\alpha}^p$ mJy beam $^{-1}$	$V_{lsr, H40\alpha}$ km s $^{-1}$	$\Delta V_{H40\alpha}$ km s $^{-1}$	$FWHM_{H40\alpha}$ maj(") \times min(")	$\rho_{H40\alpha}^{core}$ 10^{-2} pc
I09002-4732	G268.4225-00.8491	$2.0^{+0.7}_{-0.6}$	4.6×4.0	15.8	4.5×3.6	3058.0 ± 29.0	329.7 ± 2.9	$2.0^{+0.6}_{-0.5}$	242.7 ± 1.5	-2.0 ± 1.6	34.5 ± 1.6	4.4×3.3	$1.9^{+0.6}_{-0.7}$
I12320-6122	G300.9688+01.1475*	$3.1^{+0.6}_{-0.5}$	2.6×2.4	11.2	1.6×0.9	477.4 ± 9.5	333.5 ± 4.3	$0.9^{+0.2}_{-0.1}$	191.6 ± 2.0	-41.4 ± 1.6	37.3 ± 1.6	1.5×0.7	$0.8^{+0.2}_{-0.1}$
I12326-6245	G301.1364-00.2257*	$5.6^{+0.5}_{-0.4}$	2.9×2.2	172.0	1.8×1.0	2003.0 ± 49.0	1351.0 ± 21.0	$1.8^{+0.1}_{-0.1}$	526.5 ± 3.2	-63.8 ± 1.6	55.0 ± 1.6	1.6×0.8	$1.6^{+0.1}_{-0.1}$
I12383-6128	G301.7314+01.1033	$2.8^{+0.8}_{-0.6}$	4.1×3.7	17.0	3.3×3.2	96.7 ± 2.2	27.4 ± 0.5	$2.2^{+0.3}_{-0.2}$	32.8 ± 0.9	-38.3 ± 1.6	24.7 ± 1.6	3.2×2.3	$1.9^{+0.2}_{-0.1}$
I12572-6316	G303.9302-00.6879*	$11.5^{+0.3}_{-0.3}$	2.8×2.3	7.3	1.5×1.3	48.2 ± 1.0	32.3 ± 0.5	$3.9^{+0.1}_{-0.1}$	17.9 ± 0.8	24.0 ± 1.6	24.5 ± 1.6	1.4×1.0	$3.2^{+0.1}_{-0.1}$
I13080-6229	G305.1961+00.0331*	$2.3^{+0.6}_{-0.5}$	12.6×8.9	78.0	12.5×8.6	2014.0 ± 46.0	76.6 ± 1.7	$5.8^{+1.5}_{-1.4}$	70.0 ± 1.8	-35.8 ± 1.6	28.0 ± 1.6	9.3×5.2	$3.9^{+1.0}_{-0.4}$
I13291-6249	G307.5605-00.5870	$7.8^{+0.5}_{-0.4}$	7.6×5.9	24.2	7.3×5.6	562.4 ± 9.3	53.1 ± 0.8	$12.1^{+0.8}_{-0.7}$	51.0 ± 1.5	-38.2 ± 1.6	28.6 ± 1.6	4.4×3.2	$7.1^{+0.4}_{-0.4}$
I13471-6120	G309.9206+00.4788*	$6.6^{+0.6}_{-0.5}$	2.4×1.9	71.9	1.0×1.0	848.0 ± 10.0	$1.6^{+0.1}_{-0.1}$	$1.6^{+0.1}_{-0.1}$	347.8 ± 1.8	-57.0 ± 1.6	34.1 ± 1.6	1.1×1.0	$1.6^{+0.1}_{-0.1}$
I14013-6105	G311.6273+00.2902	$3.5^{+0.9}_{-0.5}$	5.0×4.8	155.0	4.8×4.3	1198.0 ± 34.0	171.0 ± 4.3	$3.9^{+0.3}_{-0.3}$	133.1 ± 1.5	-58.3 ± 1.6	37.6 ± 1.6	4.1×3.0	$3.0^{+0.1}_{-0.1}$
I14050-6056	G312.1084+00.3093	$3.1^{+0.5}_{-0.5}$	5.4×4.8	78.3	5.0×4.5	487.0 ± 16.0	63.3 ± 1.9	$3.5^{+0.6}_{-0.6}$	50.7 ± 2.0	-46.5 ± 1.6	41.0 ± 1.6	3.5×2.6	$2.2^{+0.4}_{-0.4}$

NOTE: The * symbol after the core name indicates that this core is associated with a COM-containing core or COM-containing cores. $FWHM$ is the measured core size while $FWHM_{dec}$ is the corresponding deconvolved size. R_{core} follows the form of $R_{eff}/3600 \times \pi/180 \times D$, where R_{eff} is the effective radius equal to $\sqrt{FWHM_{dec}/2}$, and D is the distance of the core. The errors on R_{core} and $R_{H40\alpha}^{core}$ mainly result from the distance uncertainties and those on the fluxes arise from the 2D Gaussian fitting in the core extraction. Only a small portion of the data is provided here and the full table will be available as supplementary material.

Table 2. Parameters of the COM-containing but not H/UC-HII-associated cores with $N_{line} \geq 20$ (or pure s-cHMC).

Name Clump	Gal. Name Core	D kpc	$FWHM$ maj(") \times min(")	PA deg	$FWHM_{dec}$ maj(") \times min(")	F_{3mm}^{int} mJy	F_{3mm}^p mJy beam $^{-1}$	R_{core} 10^{-2} pc	N_{line}	$\log(M_{core})$ M_{\odot}	$\log(n_{core})$ cm $^{-3}$	Σ_{core} g cm $^{-2}$
I08303-4303	G261.6444-02.0890	$2.4^{+0.5}_{-0.6}$	2.3×2.1	58.0	1.9×1.5	18.2 ± 0.8	7.0 ± 0.2	$1.0^{+0.2}_{-0.2}$	28	$1.1^{+0.7}_{-0.7}$	$6.6^{+3.9}_{-3.9}$	8.2
I08470-4243	G263.2500+00.5137	$2.4^{+0.6}_{-0.6}$	2.6×2.1	147.6	2.1×1.5	38.0 ± 0.9	13.5 ± 0.2	$1.0^{+0.2}_{-0.2}$	61	$1.4^{+1.1}_{-1.1}$	$6.8^{+4.2}_{-4.2}$	15.6
I13134-6242	G305.7992-00.2447	$2.0^{+0.6}_{-0.4}$	3.4×2.7	171.5	2.4×2.1	103.8 ± 2.4	47.2 ± 0.8	$1.1^{+0.3}_{-0.2}$	48	$1.7^{+1.5}_{-1.3}$	$7.0^{+4.2}_{-4.1}$	26.6
I13484-6100	G310.1436+00.7598	$6.9^{+0.7}_{-0.7}$	3.5×3.2	77.0	2.8×2.7	41.1 ± 1.7	13.0 ± 0.4	$4.6^{+0.3}_{-0.3}$	36	$2.4^{+1.5}_{-1.5}$	$5.9^{+3.9}_{-4.0}$	7.0
I14498-5856	G318.0482+00.0863	$2.9^{+0.4}_{-0.3}$	5.2×2.6	48.3	4.0×2.0	9.1 ± 0.0	4.2 ± 0.2	$2.0^{+0.3}_{-0.2}$	33	$0.9^{+0.4}_{-0.3}$	$5.8^{+3.1}_{-3.1}$	1.5
I14498-5856	G318.0497+00.0868	$2.9^{+0.4}_{-0.3}$	3.9×3.0	63.4	3.5×2.4	60.7 ± 1.4	15.9 ± 0.3	$2.0^{+0.3}_{-0.2}$	39	$1.8^{+1.2}_{-1.1}$	$6.4^{+3.7}_{-3.6}$	9.3
I15394-5358	G326.4747+00.7030	$2.4^{+0.3}_{-0.2}$	5.2×4.4	140.9	4.9×4.0	226.7 ± 5.4	28.4 ± 0.6	$2.5^{+0.3}_{-0.2}$	33	$2.2^{+1.6}_{-1.4}$	$6.6^{+3.6}_{-3.5}$	14.9

NOTE: The parameters $FWHM$, $FWHM_{dec}$, and R_{core} are derived in the same way as in Table 1. The errors on R_{core} , M_{core} and n_{core} mainly result from the distance uncertainties, and those on the fluxes from the 2D Gaussian fitting in the core extraction. Only a small portion of the data is provided here and the full table will be available as supplementary material.

Table 3. Parameters of the COM-containing but not H/UC-HII-associated cores with $5 \leq N_{line} < 20$ (or pure w-cHMC).

Name Clump	Gal. Name Core	D kpc	$FWHM$ maj(") \times min(")	PA deg	$FWHM_{dec}$ maj(") \times min(")	F_{3mm}^{int} mJy	F_{3mm}^p mJy beam $^{-1}$	R_{core} 10^{-2} pc	N_{line}	$\log(M_{core})$ M_{\odot}	$\log(n_{core})$ cm $^{-3}$	Σ_{core} g cm $^{-2}$
I08448-4343	G263.7737-00.4326	$1.4^{+0.6}_{-0.8}$	3.5×2.3	113.0	3.1×2.0	5.6 ± 1.2	1.3 ± 0.2	$0.9^{+0.4}_{-0.5}$	9	$0.1^{+0.1}_{-0.1}$	$5.9^{+2.9}_{-3.0}$	1.2
I09018-4816	G269.1523-01.1279	$2.8^{+0.6}_{-0.7}$	4.3×2.7	178.5	4.1×2.2	51.9 ± 2.1	8.6 ± 0.3	$2.1^{+0.4}_{-0.5}$	12	$1.7^{+1.3}_{-1.4}$	$6.3^{+3.8}_{-3.8}$	7.4
I10365-5803	G286.2074+00.1698	$3.4^{+0.6}_{-0.6}$	3.6×3.0	81.9	3.1×2.5	31.7 ± 1.0	9.2 ± 0.2	$2.3^{+0.4}_{-0.4}$	10	$1.6^{+1.2}_{-1.2}$	$6.1^{+3.7}_{-3.7}$	5.3
I11298-6155	G293.8274-00.7461	$9.4^{+0.4}_{-0.4}$	4.0×3.0	92.8	3.6×2.3	41.8 ± 1.9	11.8 ± 0.4	$6.6^{+0.3}_{-0.3}$	10	$2.6^{+1.6}_{-1.6}$	$5.7^{+3.8}_{-3.7}$	6.5
I11332-6258	G294.5115-01.6213	$1.1^{+0.7}_{-0.6}$	5.9×4.7	81.2	5.6×4.2	30.5 ± 2.0	3.8 ± 0.2	$1.3^{+0.8}_{-0.7}$	6	$0.6^{+0.7}_{-0.7}$	$5.9^{+2.8}_{-2.8}$	1.7
I12326-6245	G301.1363-00.2235	$5.6^{+0.5}_{-0.8}$	3.4×2.1	178.0	2.3×1.1	212.0 ± 52.0	130.0 ± 21.0	$2.2^{+0.3}_{-0.3}$	7	$2.9^{+2.1}_{-2.1}$	$7.1^{+4.9}_{-4.9}$	108.1
I13079-6218	G305.2084+00.2060	$3.0^{+0.6}_{-0.7}$	3.5×3.0	22.8	2.8×2.2	97.0 ± 2.6	39.1 ± 0.8	$1.8^{+0.4}_{-0.4}$	11	$2.0^{+1.6}_{-1.7}$	$6.7^{+4.2}_{-4.3}$	20.3
I13079-6218	G305.2022+00.2072	$3.0^{+0.6}_{-0.7}$	3.5×3.2	105.0	3.0×2.0	20.5 ± 2.8	7.8 ± 0.8	$1.8^{+0.4}_{-0.4}$	11	$1.3^{+0.9}_{-1.0}$	$6.0^{+3.5}_{-3.6}$	4.4

NOTE: The parameters $FWHM$, $FWHM_{dec}$, and R_{core} are derived in the same way as in Table 1. The errors on R_{core} , M_{core} and n_{core} mainly result from the distance uncertainties, and those on the fluxes from the 2D Gaussian fitting in the core extraction. Only a small portion of the data is provided here and the full table will be available as supplementary material.

remaining 90 COM-containing cores are cHMCs and they all are thus treated as HMC candidates for simplicity.

To make a robust sample of cHMCs, the 138 COM-containing cores are divided into two groups of cHMCs using the values of N_{line} . As shown in Fig. 5, one group, regarded as strong-cHMCs (s-cHMCs), contains 56 high-level COM-containing cores with $N_{line} \geq 20$, and the other group, regarded as weak-cHMCs (w-cHMCs), contains 82 low-level COM-containing cores with $5 \leq N_{line} < 20$. In each group, there are 24 cHMCs associated with H/UC-HII cores. The threshold $N_{line} = 20$ is somewhat arbitrary, based on our visual inspection of the spectra of all cHMCs, but does not matter too much in the following statistical analysis. Moreover, to distinguish the cHMCs between with H/UC-HII and without H/UC-HII cores, 32 pure s-cHMCs and 58 pure w-cHMCs are separated from the entire sample of the 138 cHMCs (see Fig. 5), and compiled into the two catalogues, one called pure s-cHMCs and the other one pure w-cHMCs. That is, pure cores refer to those with-

out H/UC-HII signatures. The parameters of the two catalogues are tabulated in Table 2 for pure s-cHMCs, and in Table 3 for pure w-cHMCs, including the clump and core names (Cols. 1–2), the measured sizes of the major and minor axes and the position angle (Cols. 4–5), the deconvolved sizes of both axes (Cols. 6), the core-integrated 3 mm flux (Col. 7), the core-peak flux (Col. 8), the radius (Col. 9), the number of lines (Col. 10), the mass (Col. 11), the number density (Col. 12), and the mass surface density (Col. 13). The last three parameters were calculated following the equations in Appendix B for a fixed temperature of 100 K typical of a hot core. The median radius is 1.6×10^{-2} pc in an interquartile range (IQR)⁴ of $[1.0, 2.3] \times 10^{-2}$ pc for the catalogue of 32 pure s-cHMCs, and 2.6×10^{-2} pc in an IQR of $[1.7, 5.2] \times 10^{-2}$ pc for the catalogue of

⁴ The interquartile range is a measure of statistical dispersion, being equal to the difference between 75th and 25th percentiles, or between upper and lower quartiles.

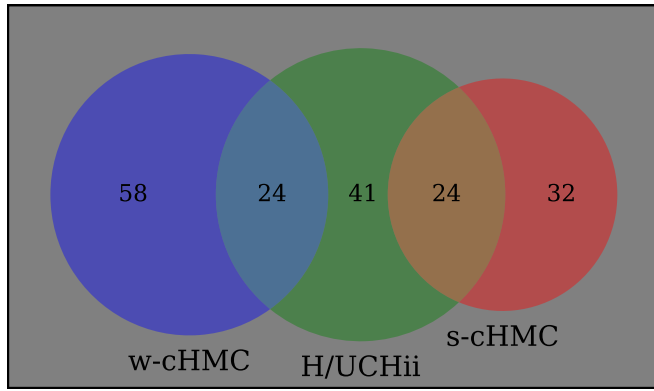


Figure 5. Venn diagram showing the relation between 138 COM-containing and 89 H/UC-HII cores. The 138 COM-containing cores consist of 58 pure and 24 H/UC-HII-associated w-cHMCs and 32 pure and 24 H/UC-HII-associated s-cHMCs.

58 pure w-cHMCs. These results suggest that most of the 90 COM-containing cores are indeed compact.

Note that contamination from free-free radiation to continuum may not be trivial for the cores associated with H/UC-HII. In practice, we calculated at a temperature of 100 K the masses for two types of cores, pure cHMCs and cHMCs associated with H/UC-HII sources (i.e., compact H40 α emission). In comparison, we found that the mass of the latter cores ($\sim 10^4 M_{\odot}$) is on average about two magnitude higher than that of the former cores ($\sim 10^2 M_{\odot}$). This result suggests that contamination by free-free radiation is non-negligible in calculating the flux-related parameters. Since this contamination cannot be accurately determined, we do not give the estimate of the continuum flux-related parameters for the H/UC-HII cores such as the mass.

3.3 Compact dense core list not associated with either cHMC or H/UC-HII.

As described above, we extract 453 cores in 3 mm continuum. Of these, 89 are classified as H/UC-HII, 32 as s-cHMC, and 58 as w-cHMC. The remaining 274 cores lack observationally-quantifiable metrics for association into any of the three categories above. Hence we refer to these as “unknown cores” (see Table 4). These “unknown cores” could be simple continuum flux condensations in an earlier evolutionary stage. Indeed, chemically poor HMPOs and candidate massive prestellar cores have been detected in some massive proto-clusters (e.g., Liu et al. 2017). However, it is also possible that some (to date) unknown but potentially significant fraction of these “unknown cores” may actually be cHMC or H/UC-HII cores that fall below our sensitivity limit due to spatial resolution, distance, and/or flux limitations. These will be investigated in more detail in future work.

For reference, the mass, number density, and mass surface density of the “unknown” cores (see Table 4), were calculated (see Appendix B) assuming a dust temperature of 25 K. This temperature is comparable to the median value of the clumps that do not have cHMC or H/UC-HII signatures. As a result, these cores have a median radius of 2.4×10^{-2} pc in an IQR of $[1.3, 4.6] \times 10^{-2}$ pc, a median mass of $19 M_{\odot}$ in an IQR of $[5, 99] M_{\odot}$, a median number density of $0.6 \times 10^6 \text{ cm}^{-3}$ in an IQR of $[0.3, 1.3] \times 10^6 \text{ cm}^{-3}$, and a median mass surface density of 2.2 g cm^{-2} in an IQR of $[1.1,$

$4.3] \text{ g cm}^{-2}$. The properties of the “unknown” cores will be more thoroughly investigated in a forthcoming paper.

4 DISCUSSION

4.1 Limitations in dense core extraction and classification

Our ATOMS survey consists of a uniform sensitivity and angular resolution survey toward regions located over a large range of distances. Consequently, the dense core extraction, as discussed above, is affected by variations of factors of order of ~ 10 in distance across the sample. Here we focus on the most robust (brightest) portion of our sample (i.e. w-cHMC, s-cHMC and H/UC-HII cores, see Sect. 3.2).

Figure 6 shows how the radii (R) and masses (M) depend on distances (D) for the three groups (w-cHMC, s-cHMC and H/UC-HII) of dense cores. There are clear increasing trends in R vs. D and M vs. D relations, further suggesting that distant sources were not well resolved. With future higher resolution observations, we expect that these distant cores with sizes of ~ 0.1 pc would break down to smaller sub-cores or condensations with sizes of ~ 0.01 pc. Moreover, the masses of the w-cHMC and s-cHMC cores can be found in Figure 6b far above the detection limit, which is in agreement with the nature of bright emission in continuum for those two types of cores.

Moreover, beam dilution impairs detection of hot and H/UC-HII cores at large distances. Therefore, we assume a smaller detection rate of such cores at larger distances. We tested this assumption by re-examining the detectability of the COM and H40 α lines after pushing the observations of the relatively nearby sources to a large distance. In practice, we smoothed the cubes of SPWs7–8 for 10 cHMCs and 5 H/UC-HII cores at distances ≤ 2 kpc to the larger beam size that was transferred from the ATOMS typical angular resolution ($\sim 1.6''$) at a fixed far distance of 5 kpc. In consequence, only 30% of the selected cHMC sources were re-identified using the same HMC identification method as in Sect. 3.2.2, while 80% of the selected H/UC-HII sources have been re-identified. This result suggests that beam dilution affects the detectability for cHMCs more than it does for H/UC-HII cores at the ATOMS sensitivity.

Furthermore, Fig. 7 shows the distance distributions of three groups of clumps, which contain w-cHMC, s-cHMC and H/UC-HII. For comparison, we also plot the distance distribution of the full sample. Indeed, we find that the candidate hot cores (w-cHMC and s-cHMC) tend to be located at nearer distances (Fig. 7b,c), with their cumulative distribution curves (in red and blue colors in Fig. 7a) above the curve (in gray color) for the full sample.

We test whether the distance distributions of clumps containing different kinds of dense cores follow the same distribution as the full sample with Kolmogorov-Sminov test. The unknown hypothesis is that two distributions follow the same distribution. The tests are consistent with the unknown hypothesis for the w-cHMCs group (P-value=0.37) and H/UC-HII group (P-value=0.67) due to their P-values being greater than 0.05, suggesting that the detection rates of w-cHMCs and H/UC-HII are not greatly affected by the distance issue. In contrast, the P-value for s-cHMCs is 0.06, indicating that the detection of s-cHMCs is significantly limited by distances. It may imply that the detection rate of s-cHMCs is significantly underestimated for distant sources. This is in line with the cumulative distribution function of distances (Fig. 7a). In the figure, clumps with s-cHMC appear to show smaller distances (~ 2.6 kpc on average) than those (~ 3.2 kpc on average) with w-cHMC, indicating that the detection of hot cores at large distances is incomplete.

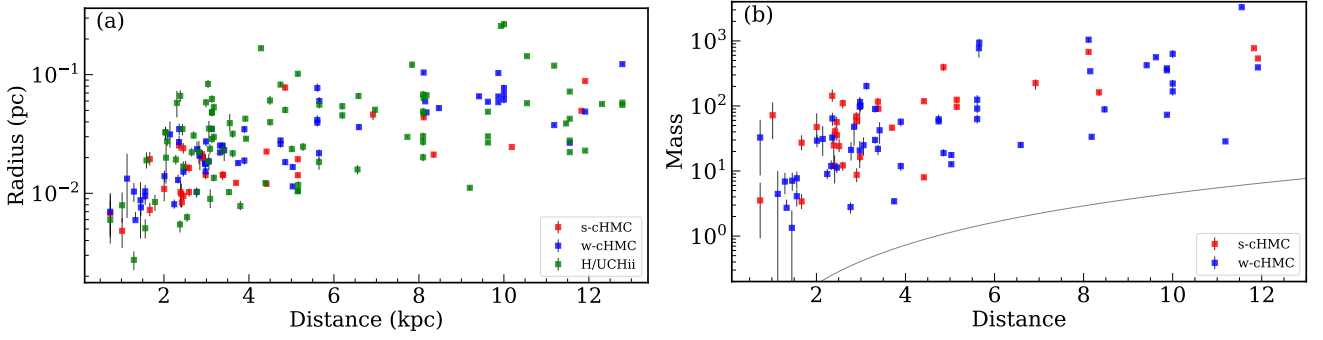


Figure 6. (a): Radius versus distance for w-cHMC, s-cHMC, and H/UC-HII cores. The p value of the KS test 0.03 suggests that the size distributions of w-cHMC and s-cHMC come from an identical distribution. (b): Mass versus distance for w-cHMC, and s-cHMC cores. H/UC-HII cores are not shown here since their masses cannot be estimated from 3 mm continuum due to free-free contamination (see text in Sect. 3.2.2). The curve is the mass sensitivity distribution as a function of the distance.

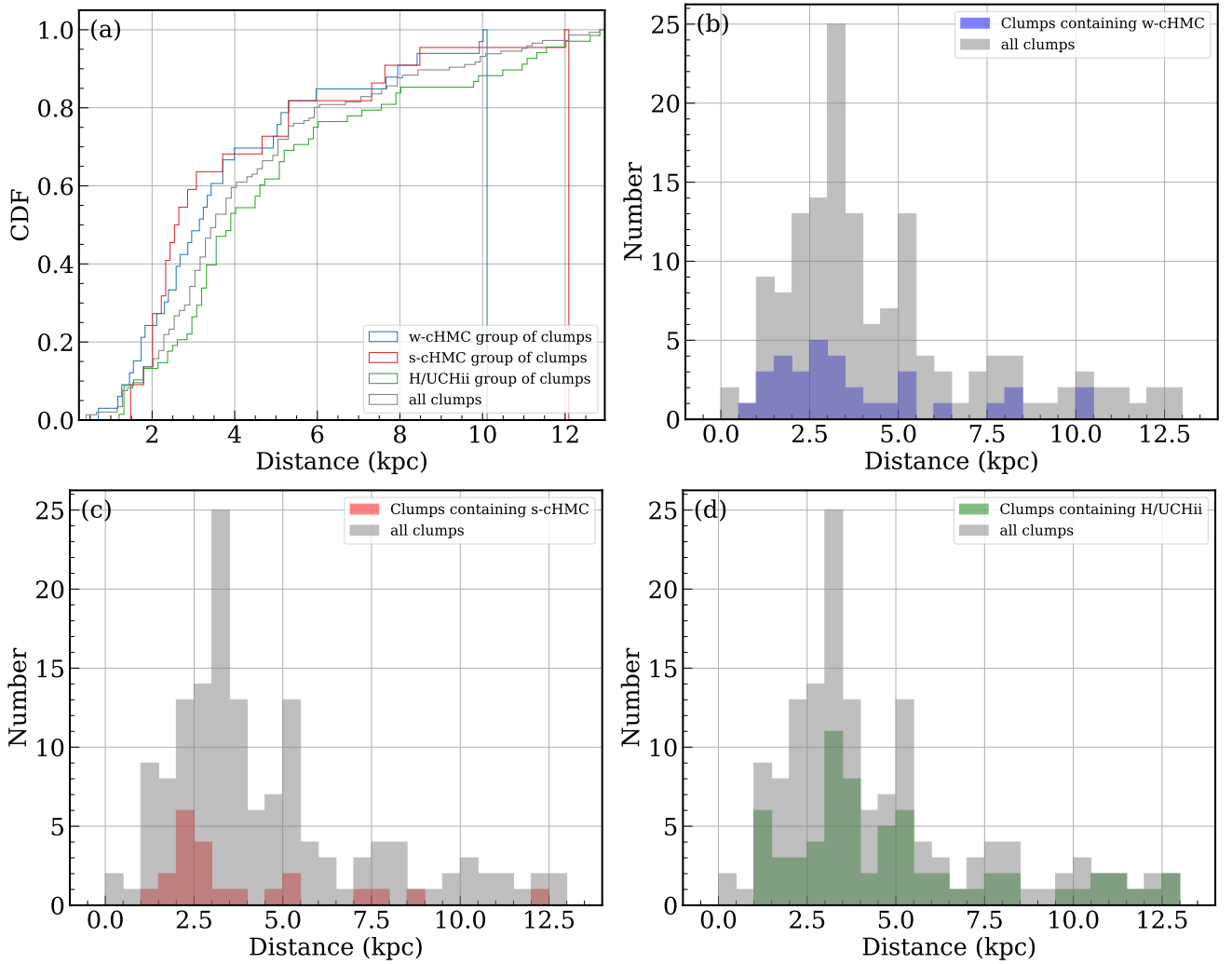


Figure 7. Distance distribution of the four groups of clumps. (a): cumulative distribution function. (b–d): histograms of all clumps against w-cHMC group, s-cHMC group, and H/UC-HII group of clumps, respectively.

Table 4. Parameters of the “unknown” cores (i.e., no signature of H/UC-HII nor cHMC)

Name Clump	Gal. Name Core	D kpc	$FWHM$ maj(") \times min(")	PA deg	$FWHM_{dec}$ maj(") \times min(")	$F_{3mm}^{int.}$ mJy	F_{3mm}^p mJy beam $^{-1}$	R_{core} 10^{-2} pc	$\log(M_{core})$ M_{\odot}	$\log(n_{core})$ cm $^{-3}$	Σ_{core} g cm $^{-2}$
I08076-3556	G253.2971-01.6156	$1.0^{+0.5}_{-0.5}$	5.1×3.3	86.4	4.9×3.0	11.6 ± 1.2	1.3 ± 0.1	$0.9^{+0.4}_{-0.5}$	$0.1^{+0.1}_{-0.1}$	$5.9^{+2.5}_{-2.6}$	0.9
I08076-3556	G253.2930-01.6113	$1.0^{+0.5}_{-0.5}$	2.2×1.6	99.3	1.6×1.1	18.8 ± 0.5	9.8 ± 0.2	$0.3^{+0.1}_{-0.1}$	$0.3^{+0.3}_{-0.3}$	$7.2^{+3.9}_{-4.0}$	13.0
I08303-4303	G261.6446-02.0899	$2.4^{+0.5}_{-0.5}$	4.9×2.5	6.9	4.7×2.0	23.7 ± 1.4	3.6 ± 0.2	$1.8^{+0.4}_{-0.4}$	$1.1^{+0.8}_{-0.8}$	$6.0^{+3.3}_{-3.1}$	2.9
I08303-4303	G261.6444-02.0876	$2.4^{+0.5}_{-0.5}$	4.0×3.8	40.0	3.8×3.5	15.2 ± 1.6	1.8 ± 0.2	$2.1^{+0.5}_{-0.5}$	$1.0^{+0.6}_{-0.6}$	$5.7^{+3.0}_{-3.0}$	1.3
I08448-4343	G263.7776-00.4332	$1.4^{+0.6}_{-0.6}$	5.2×3.0	116.0	5.0×2.8	8.8 ± 1.7	1.1 ± 0.2	$1.3^{+0.6}_{-0.7}$	$0.3^{+0.2}_{-0.3}$	$5.6^{+2.7}_{-2.8}$	0.7
I08448-4343	G263.7729-00.4364	$1.4^{+0.6}_{-0.6}$	2.5×1.8	72.0	2.1×1.1	2.1 ± 0.8	0.9 ± 0.2	$0.5^{+0.2}_{-0.3}$	$-0.3^{+0.4}_{-0.3}$	$6.0^{+3.0}_{-3.1}$	1.1
I08448-4343	G263.7724-00.4366	$1.4^{+0.6}_{-0.6}$	2.2×1.8	103.0	1.5×1.3	1.9 ± 0.7	0.9 ± 0.2	$0.5^{+0.2}_{-0.3}$	$-0.4^{+0.5}_{-0.4}$	$6.0^{+3.0}_{-3.1}$	1.1
I08448-4343	G263.7723-00.4350	$1.4^{+0.6}_{-0.6}$	4.4×2.2	80.6	3.6×1.8	7.3 ± 0.0	5.8 ± 0.2	$0.9^{+0.5}_{-0.5}$	$0.2^{+0.1}_{-0.2}$	$6.5^{+3.7}_{-3.7}$	1.3
I08448-4343	G263.7744-00.4328	$1.4^{+0.6}_{-0.6}$	2.5×2.2	18.0	2.1×1.6	11.5 ± 0.9	3.9 ± 0.2	$0.6^{+0.3}_{-0.3}$	$0.4^{+0.3}_{-0.4}$	$6.5^{+3.5}_{-3.6}$	3.9
I08448-4343	G263.7712-00.4363	$1.4^{+0.6}_{-0.6}$	3.2×1.8	157.0	2.9×1.1	2.4 ± 0.9	0.8 ± 0.2	$0.6^{+0.3}_{-0.3}$	$-0.3^{+0.4}_{-0.3}$	$5.8^{+3.6}_{-2.9}$	0.9

NOTE: The parameters $FWHM$, $FWHM_{dec}$, and R_{core} are derived in the same way as in Table 1. The errors on R_{core} , M_{core} and n_{core} mainly come from the distance uncertainties, those on the fluxes from the 2D Gaussian fitting in the core extraction. Only a small portion of the data is provided here, and the full table will be available as supplementary material.

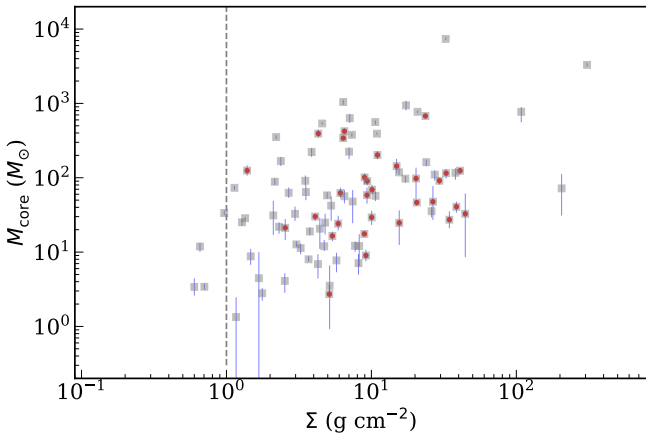


Figure 8. Distributions of the mass and mass surface density of the 90 COM-containing cores that are not associated the H/UC-HII signature. The two parameters were calculated assuming a temperature of 100 K typical of HMCs (see Appendix B). The dashed vertical line indicates a stringent theoretical threshold of 1 g cm^{-2} above which the cores most likely form high-mass stars. The red dots highlight the cores associated with the Class II CH_3OH masers, showing that they are widely distributed, but above the 1 g cm^{-2} line.

4.2 Nature of the COM-containing and not H/UC-HII-associated cores

Since emission in the COM transitions covered by the ATOMS observations can be detected towards several distinct objects, including low/high-mass prestellar cores, HMPO cores, HMCs, and even hot corinos associated with low-mass protostars (e.g., Vastel et al. 2014; Jiménez-Serra et al. 2016; Soma et al. 2018; Csengeri et al. 2019; Molet et al. 2019; Jorgensen, Belloche, & Garrod 2020; Hsu et al. 2020), it is necessary to constrain the nature of the 90 COM-containing cores that are not associated with H/UC-HII (see Sect. 3.2.2). To this end, we investigate the distribution of both the mass (M_{core}) and the mass surface density (Σ_{core}) of the 90 COM-containing cores, as shown in Fig. 8. They have a median value of mass equal to $\sim 57 M_{\odot}$ in an IQR of $19\text{--}138 M_{\odot}$, and surface densities with a median value of $\sim 6.5 \text{ g cm}^{-2}$ in an IQR of 3.3 to 15.6 g cm^{-2} .

Theoretically, cores (on scale $< 0.1 \text{ pc}$) with $\Sigma_{crit} \geq 1 \text{ g cm}^{-2}$ will most likely form high-mass stars (Krumholz & McKee 2008).

Searching from existing maser catalogue⁵(Ladeyschikov, Bayandina, & Sobolev 2019), we find that $\sim 34\%$ of the 90 COM-containing cores are associated with Class II CH_3OH masers located within the core size (red dots in Fig. 8). Class II CH_3OH masers have been found to be exclusively associated with high mass star forming regions (e.g., Cyganowski et al. 2009). The spread of Σ_{core} for the cores associated with the CH_3OH masers is consistent with the theoretical prediction (i.e., the red dots versus the vertical dashed line in the figure). Following the threshold $\Sigma_{crit} \geq 1 \text{ g cm}^{-2}$, we find that $\sim 96\%$ of the 90 COM-containing cores above it will most likely form high-mass stars. We note that there are six COM-containing cores, three of which are associated with Class II masers, above the threshold but with $M_{core} < 10 M_{\odot}$. We suggest that these cores could have been in the process of forming high-mass stars for a significant fraction of their lifetime, so that a large fraction of their mass has been accreted onto the central HMPOs. We also note that if the actual temperature of the 90 COM-containing cores is lower than 100 K, the possibility that they form high-mass stars will be higher. For reference, if the temperature is assumed to be 50 K, the mass and surface density will be about two times higher.

Overall, the probability that the identified COM-containing cores are associated with low-mass star forming objects (i.e., low-mass prestellar cores, and hot corinos) is rather low. Given that emission in the COMs transitions available in the ATOMS data has been already observed towards other HMPO and HMC regions (Csengeri et al. 2019; Jorgensen, Belloche, & Garrod 2020), we conclude that most (if not all) of the 90 COM-containing cores should be either HMPO cores or HMCs. Note that HMPOs are simply assumed here to be younger than HMCs although this timescale relation has yet to be determined.

To distinguish definitely between the two types of high-mass star-forming cores requires knowledge of their temperatures. The temperature is usually computed from a rotational diagram analysis of multiple transitions of one or more COM species (e.g., CH_3OCHO , and CH_3OH). However, the range of upper level energy of the COM lines covered in the ATOMS survey is too narrow to permit a reliable temperature determination. This thus requires follow-up observations of higher frequency transitions that arise from higher energy levels. For simplicity, hereafter, we treat the 90 COM-containing cores as cHMCs (see Sect. 3.2.2) since the detection rate of COMs towards HMCs is presumably higher than towards HMPOs.

In short, most of the 90 COM-containing cores are presumably

⁵ <http://maserdb.net/download.pl>

in the very early stages of high-mass star formation. We include them in two separate catalogues: one including 32 s-cHMCs and the other including 58 w-cHMCs, with the former catalogue presumably containing more robust HMCs candidates than the latter. These catalogues constitute a unique database of objects for future follow-up higher-resolution observations to investigate the dynamical processes related to high-mass star formation, such as infall, outflow, and rotation.

4.3 Constraints on the Duration of the HMC Phase

Because heating by the forming star precedes ionization, the general picture is that HMCs precede H/UC-HII in the evolution of a core to a massive star (Garay & Lizano 1999; Kurtz et al. 2000; van der Tak 2004; Cesaroni 2005; Rathborne et al. 2011). Our large sample, unbiased towards either HMCs or H/UC-HII cores, enables further study. First, the two phenomena are not exclusive, as there is a substantial overlap between HMCs and H/UC-HII (Fig. 5). Nearly half (48/89) of H/UC-HII in the sample show COMs, indicating that hot cores may persist during nearly half of H/UC-HII lifetime even when the central high-mass protostars start to ionize the surroundings.

Second, with certain assumptions, we can use the numbers of candidate HMCs and cores with H/UC-HII to estimate the relative duration of the HMC phase. For a rigorous result, the survey must be complete, the evolution through the phases must be a continuous process proceeding at a steady rate for a period longer than the last phase considered, and other variables, such as the mass of the star, cannot be important. Further study of this sample is needed to check these assumptions, so we offer here only some preliminary considerations.

As discussed in Sect. 4.1, the ATOMS survey is more complete in the detection of H/UC-HII regions than HMCs, so we have a lower limit on the number counts of HMCs. The total number (138) of COM-containing dense cores (w-CHMC and s-CHMC) is already larger than the number (89) of H/UC-HII cores. The number of strong candidate HMCs (56) is smaller than the number (89) of H/UC-HII cores but may be greatly underestimated due to the distance effect. The most important unknown is the mass of the forming star because the number of ionizing photons is a very strong function of stellar mass. If all these cores will form stars capable of producing a H/UC-HII, the current lack of one is due to evolution. Further study of the luminosity of the individual cores with JWST observations could test this assumption.

With all these caveats, we suggest that the duration of candidate hot cores is at least comparable to the lifetime of H/UC-HII and is probably greater.

4.4 The origin of chemical differentiation among high-mass star forming cores

Some high-mass star forming cores are found to be chemically rich while others are not. Even cHMCs show differing richness in molecular lines especially in COMs. The median N_{line} values are 8 within an IQR of [5, 16] for the 58 w-cHMCs, and 57 within an IQR of [28, 123] for the 32 s-cHMCs. Would this different chemical richness (i.e., N_{line}) be related to an evolutionary sequence from w-cHMCs \rightarrow s-cHMCs?

The chemical differentiation among high-mass star forming cores could be partially attributed to an evolutionary effect. More evolved cores with higher luminosity can heat a larger volume of their surroundings, evaporating molecules from ices and thus increasing the gaseous molecular abundances.

The 146 analyzed ATOMS clumps can be classified into four main groups according to the types of cores they harbour: (i) the w-cHMC group with 28 clumps hosting w-cHMC cores, (ii) the s-cHMC group with 17 clumps hosting s-cHMC cores, (iii) the H/UC-HII group with 68 clumps containing H/UC-HII cores, and (iv) the “unknown” group with 28 clumps without cHMC or H/UC-HII cores. There are five clumps with both w-cHMC and s-cHMC cores. Note that if a clump hosts both H/UC-HII core and cHMC, it will be placed into the H/UC-HII group. In addition, the w-cHMC group could contain s-cHMC cores that are not detectable yet or appear as w-cHMC cores due to the limited angular resolution and sensitivity. That is, there could be an underlying overlap between w-cHMC and s-cHMC groups of clumps, so the following analysis should be treated with caution. To explore the evolutionary stage of the clumps in the different groups we resort to two parameters available for the ATOMS clumps (see Paper I): the bolometric luminosity to mass ratio $L_{\text{bol}}/M_{\text{clump}}$ and the dust temperature T_d . These parameters, which cannot be directly determined for the cores with the ATOMS data alone, are distance independent and have been proposed as indicator of the evolutionary stage of clumps (e.g., Guzmán et al. 2015).

Figure 9 plots the distribution of the two parameters for the four groups of clumps. The “unknown”, w-cHMC, s-cHMC, and H/UC-HII groups have respective median L/M values 28.1, 26.9, 29.7, $32.7 L_{\odot}/M_{\odot}$. These values fall into the range of $2 \leq L/M \leq 40 L_{\odot}/M_{\odot}$ observationally defined for the high-mass star-forming objects (Giannetti et al. 2017; Elia et al. 2017). This result suggests that the four groups of clumps harbour embedded phases of high-mass star formation. As such, many of the clumps in the “unknown” group could not be really devoid of high-mass star-forming cores, and instead harbour HMPO objects or even more evolved HMC that could not be detected with the sensitivity of the ATOMS data. If we only consider the w-cHMC, s-cHMC, and H/UC-HII groups, there is a weak increasing trend in the median values of the $L_{\text{bol}}/M_{\text{clump}}$ ratio. A similar, but stronger, trend also appears in the temperature distribution among these three groups of clumps.

The differences in $L_{\text{bol}}/M_{\text{clump}}$ and T_d of the natal clumps are not very significant. If the evolution from HMCs to H/UC-HII is correct for individual cores, the explanation for the poor correlation with clump-scale properties may be that the evolution of individual cores to stars within a clump differs, and the clump-scale evolution of L_{bol} is driven by the most massive/evolved core. To study evolution at the core level, higher angular resolution and sensitivity in the mid-infrared to far-infrared is needed to pinpoint the embedded protostars, which cannot be well resolved at the current resolution of the infrared data, through the spectral energy distribution over a large dynamical frequency range.

In addition, recent studies of low-mass cores indicate that chemical richness of star forming cores may not be related to evolutionary sequence. Belloche et al. (2020) suggested a luminosity threshold of $4 L_{\odot}$, above which low-mass cores should exhibit spectral features from at least one COM and may contain hot corinos. However, in a recent study of a large sample of 49 low-mass star forming cores located in the Orion complex by Hsu et al. (2020), many protostellar objects with luminosities much greater than $4 L_{\odot}$ do not show any clear sign of COMs or hot corinos. This indicates that the chemical differentiation among star forming cores depends on their chemical history, as well as their luminosity.

An alternative scenario could be that some star forming cores in their “cold” core phase form abundant molecules such as COMs on ice mantles through grain-surface chemistry while other cores do not. These different behaviours are probably related to varying physical and chemical properties as well as initial conditions of dif-

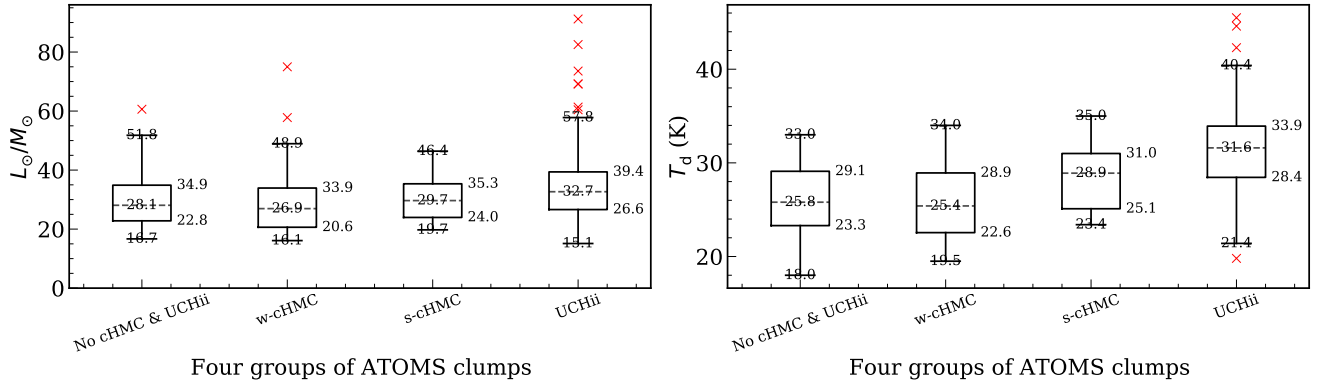


Figure 9. Box and whisker plot showing for four groups of clumps the distribution of the L/M ratio (panel a), dust temperature T_d (panel b). The numbers associated with the boxes from the top to bottom represent the upper quartile, median (inside the box), and lower quartile, respectively. The red crosses indicate the outliers outside 1.5 times the interquartile range either above the upper quartile or below the lower quartile.

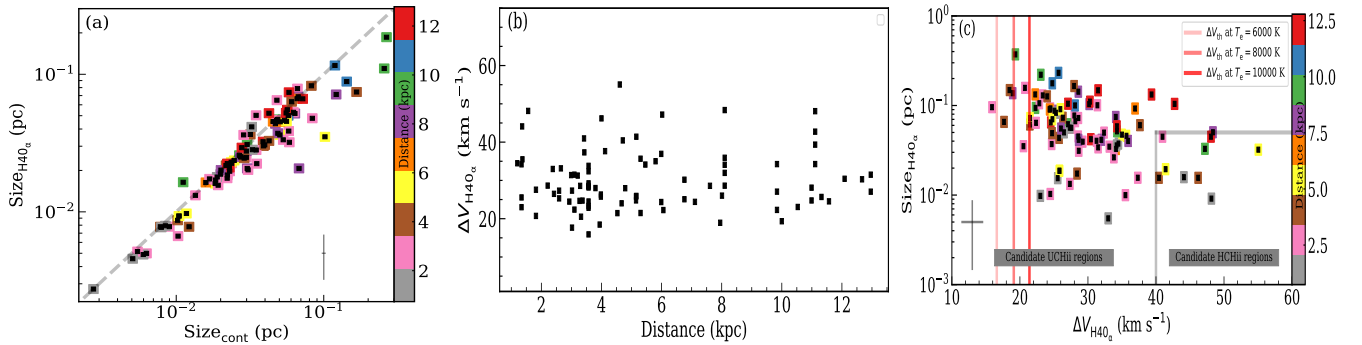


Figure 10. Size and $H_{40\alpha}$ line width of the 89 H/UC-HII cores. (a): comparison between the two types of core sizes, one measured from 3 mm continuum (in x-axis) and the other from $H_{40\alpha}$ emission (in y-axis). The color scheme encodes distance information of the cores. The typical error bars for the two measurements are presented at the bottom right. (b): distribution of the $H_{40\alpha}$ line width as a function of distance. (c): Relation between the size of the H/UC-HII cores measured from $H_{40\alpha}$ emission and the line width of $H_{40\alpha}$ ($\Delta V_{H_{40\alpha}}$). The color scheme is the same as in panel (a). The H/UC-HII cores are roughly divided into 79 UC-HII and 10 HC-HII classes. For reference, the thermal-broadening line widths are given in three color-gradient vertical lines at 16.6 km s^{-1} , 19.1 km s^{-1} , 21.4 km s^{-1} for the electronic temperatures 6,000 K, 8,000 K, and 10,000 K, respectively. The typical error bars for the two parameters are presented at the bottom left.

ferent sources. When molecules evaporate from ice in the “hot” core phase, their gaseous molecular abundances should also vary greatly. This scenario could be tested by detailed chemical studies toward a sample of “cold clumps” like in infrared dark clouds that lack active star formation and may represent the very initial conditions of high-mass star formation. Detailed chemical investigations are beyond the scope of this work. More detailed chemical studies of molecular abundances of dense cores will be presented in forthcoming papers.

4.5 Size versus $H_{40\alpha}$ linewidth relationship for H/UC-HII cores

The 89 H/UC-HII cores could be associated with either HC-HII or UC-HII regions, and we attempt to distinguish them by their observable properties (see Sect. 1). To this end, we focus on the size and line width of the radio recombination line ($\Delta V_{H_{40\alpha}}$) of the H/UC-HII cores, as shown in Fig. 10. These cores have two types of sizes, one measured from 3 mm continuum and the other one from $H_{40\alpha}$ emission. As shown in Fig. 10a, the two types of sizes match each other well until the size is greater than 0.1 pc. This result suggests that $H_{40\alpha}$ emission mainly contributes to 3 mm continuum when the H/UC-HII core size is less than 0.1 pc. From distance information of the cores as indicated in the colorscale in Fig. 10a, it can be seen

that the deviation of the two types of core sizes does not depend on the distance. We suspect that when the H/UC-HII core size is greater than 0.1 pc, more cold dust emission could be included within it, leading to an overestimation of the size of the real ionized gas region. In view of this, the size measured from $H_{40\alpha}$ emission for the 89 H/UC-HII cores will be discussed in the following. These cores have sizes from $\sim 5.3 \times 10^{-3}$ to 3.7×10^{-1} pc with a median value of 5.7×10^{-2} pc.

The $\Delta V_{H_{40\alpha}}$ of the 89 H/UC-HII cores range from ~ 15 to 55 km s^{-1} with a median value of 28 km s^{-1} . The measurement of $\Delta V_{H_{40\alpha}}$ is not found to be distance-dependent, as shown in Fig. 10b. Actually, the $\Delta V_{H_{40\alpha}}$ values are typical of both UC-HII and HC-HII regions, namely in a range of ~ 10 to 40 km s^{-1} for the former and 40 to 60 km s^{-1} or even higher for the latter (e.g., Hoare et al. 2007; Rivera-Soto et al. 2020). Following the typical size and line width of radio recombination lines of H/UC-HII regions (see above), the 89 H/UC-HII cores can be divided into 79 UC-HII and 10 HC-HII cores (see Fig. 10c). That is, most ($\sim 90\%$) of the compact-HII cores are UC-HII cores while only a small fraction ($\sim 10\%$) of them are HC-HII cores. Therefore, if the lifetime of UC-HII is of the order of 10^5 yr, the lifetime of HC-HII will be $\sim 10^4$ yr (e.g., Wood & Churchwell 1989; Davies et al. 2011).

In general, the widths of radio recombination lines are due to

a combination of thermal, dynamical, and/or pressure broadening mechanisms (e.g., Keto, Zhang, & Kurtz 2008; Nguyen-Luong et al. 2017; Rivera-Soto et al. 2020). The thermal broadening, ΔV_{th} , is given by $\Delta V_{\text{th}} = (8 \ln 2 k_B T_e / m_H)^{1/2}$ where k_B is the Boltzmann constant and m_H is the mass of the atom hydrogen. For electron temperatures of $T_e = 6,000$ K, $8,000$ K, and $10,000$ K, the respective thermal widths are 16.6 km s^{-1} , 19.1 km s^{-1} , 21.4 km s^{-1} , (see the three vertical color-gradient lines in Fig. 10c). Most ($\sim 96\%$) of the H/UC-HII cores are found to have $\Delta V_{\text{H40}\alpha}$ widths larger than $\sim 19 \text{ km s}^{-1}$, which corresponds to the thermal broadening for an electron temperature of $8,000$ K typical of an ionized plasma (e.g., Osterbrock & Ferland 2006). This result indicates that in addition to the thermal broadening, non-thermal (e.g., dynamical and/or pressure) broadening mechanisms are responsible for the observed large $\Delta V_{\text{H40}\alpha}$ in most of the 89 H/UC-HII cores.

Moreover, we find that the $\text{H40}\alpha$ line width decreases as the size of the core increases. To investigate if the trend is distance-dependent or not, we present the distance information of each H/UC-HII core in colorscale in Fig. 10. The figure shows that the decreasing trend persists rather than breaks at different distances, and thus it is physically meaningful. It indicates that non-thermal (e.g., dynamical and/or pressure) mechanisms dominate the broadening on smaller scales of the H/UC-HII cores (Garay & Lizano 1999).

5 SUMMARY AND CONCLUSION

Using the 3 mm ATOMS survey data, we searched for the presence of compact cores towards 146 IRAS clumps located within the inner galactic disk in the range $-80^\circ < l < 40^\circ$ and $|b| < 2^\circ$. The compact cores were extracted from 3 mm continuum emission maps through a combination of the *Dendrogram* algorithm and *CASA-imfit* task. The main results of this work are summarized as follows:

- We compiled three catalogues of compact cores with different characteristics. One catalogue, referred to as the H/UC-HII catalogue, includes 89 cores that enshroud H/UC-HII regions as indicated by the presence of compact $\text{H40}\alpha$ emission; a second catalogue, referred to as the pure s-cHMC catalogue, includes 32 s-cHMCs associated with a rich spectrum ($N \geq 20$ lines) of complex organic molecules (COMs); the third catalogue, referred to as the pure w-cHMC catalogue includes 58 w-cHMCs with relatively low levels of COM richness (i.e., $5 \leq N_{\text{line}} < 20$). These three catalogues of compact cores provide a crucial foundation for future studies of the early stages of high mass star formation across the Milky Way. We find that nearly half of H/UC-HII cores are candidate hot molecular cores.
- For completeness, another catalogue that includes the remaining 274 cores without the signature of either cHMC or H/UC-HII, referred to as the “unknown” catalogue, is also provided. These cores deserve future detailed investigation, since some of them could be in the evolutionary stages of high-mass star formation prior to formation of a HMC, and thus could be good targets for studying initial conditions of high-mass star formation.
- The detection rate of candidate distant hot cores is greatly underestimated due to relatively poorer linear resolution and line sensitivity than for nearer sources. However, the total number (138) of the detected COM-containing dense cores is still larger than the number (89) of H/UC-HII cores, indicating that the duration of high-mass protostellar cores (or cores) showing line-rich features could be at least comparable to the lifetime of H/UC-HII phase.
- We find weak increasing trends in L/M ratio and dust temperature (T_d) for the natal clumps that contain different kinds

of dense cores (w-cHMC \rightarrow s-cHMC \rightarrow H/UC-HII). However, the chemical classes indicating core evolution are not well traced by the $L_{\text{bol}}/M_{\text{clump}}$, suggesting that the evolution of individual cores is not captured by that evolutionary indicator used for clumps.

- Based on the relationship between size and $\text{H40}\alpha$ line width, we conclude that of the 89 H/UC-HII cores, 79 are associated with UC-HII and 10 with HC-HII regions. We also find that the width of the $\text{H40}\alpha$ line increases as the core size decreases, suggesting that non-thermal (e.g., dynamical and/or pressure) line-broadening mechanisms are dominant on the smaller scales of the H/UC-HII cores.

The 3 mm interferometric catalogues of high-mass star-forming cores provided here can be used to study the kinematics and dynamics of molecular gas in the vicinity of newly-formed (proto)OB stars and somewhat-evolved H/UC-HII regions. Such studies will definitely advance our understanding of the dynamical processes in the early stages of high-mass star formation, such as infall, outflow, and rotational motions, and our knowledge of the roles of feedback (e.g., outflows, stellar winds, and H/UC-HII regions) in the process of high-mass star-formation.

Acknowledgements

We thank the anonymous referee for comments and suggestions that greatly improved the quality of this paper. H.L. Liu acknowledges funding from a Fondecyt Postdoctoral project (code 3190161). H.L. Liu also thanks Shanghai Astronomical Observatory for providing office facilities that facilitated analysis of this work. T. Liu acknowledges the supports from the international partnership program of Chinese academy of sciences through grant No.114231KYSB20200009, National Natural Science Foundation of China (NSFC) through grant NSFC No.12073061, and Shanghai Pujiang Program 20PJ1415500. G.G. acknowledges support from ANID project AFB 170002. S.-L. Qin is supported by NSFC under No.12033005. L.B. acknowledges support from CONICYT project Basal AFB-170002. AS gratefully acknowledges funding support through Fondecyt Regular (project code 1180350) and from Chilean Centro de Excelencia en Astrofísica y Tecnologías Afines (CATA) BASAL grant AFB-170002. RA acknowledges funding support from CONICYT Programa de Astronomía Fondo ALMA-CONICYT 201731170002. This work was carried out in part at the Jet Propulsion Laboratory, which is operated for NASA by the California Institute of Technology. CWL is supported by the Basic Science Research Program through the National Research Foundation of Korea (NRF) funded by the Ministry of Education, Science and Technology (NRF-2019R1A2C1010851). K.T. was supported by JSPS KAKENHI Grant Number 20H05645. This paper makes use of the following ALMA data: ADS/JAO.ALMA#2019.1.00685.S. ALMA is a partnership of ESO (representing its member states), NSF (USA), and NINS (Japan), together with NRC (Canada), MOST and ASIAA (Taiwan), and KASI (Republic of Korea), in co-operation with the Republic of Chile. The Joint ALMA Observatory is operated by ESO, AUI/NRAO, and NAOJ. This research made use of *astrodendro*, a Python package to compute dendrograms of Astronomical data (<http://www.dendrograms.org/>). This research made use of *Astropy*, a community-developed core Python package for Astronomy (*Astropy Collaboration*, 2018).

Data availability

The data underlying this article are available in the article and in its online supplementary material.

REFERENCES

- Belloche A., Maury A. J., Maret S., Anderl S., Bacmann A., André P., Bontemps S., et al., 2020, *A&A*, 635, A198. doi:10.1051/0004-6361/201937352
- Beuther H., 2007, *IAUS*, 237, 148. doi:10.1017/S1743921307001378
- Beuther H., Schilke P., Sridharan T. K., Menten K. M., Walmsley C. M., Wyrowski F., 2002, *A&A*, 383, 892. doi:10.1051/0004-6361:20011808
- Bronfman L., Nyman L.-A., May J., 1996, *A&AS*, 115, 81
- Cesaroni R., Galli D., Lodato G., Walmsley C. M., Zhang Q., 2007, *prpl.conf*, 197
- Cesaroni R., Hofner P., Araya E., Kurtz S., 2010, *A&A*, 509, A50. doi:10.1051/0004-6361/200912877
- Cesaroni R., 2005, *IAUS*, 227, 59. doi:10.1017/S1743921305004369
- Churchwell E., 2002, *ARA&A*, 40, 27. doi:10.1146/annurev.astro.40.060401.093845
- Coletta A., Fontani F., Rivilla V. M., Mininni C., Colzi L., Sánchez-Monge Á., Beltrán M. T., 2020, *A&A*, 641, A54. doi:10.1051/0004-6361/202038212
- Csengeri T., Belloche A., Bontemps S., Wyrowski F., Menten K. M., Bouscasse L., 2019, *A&A*, 632, A57. doi:10.1051/0004-6361/201935226
- Cyganowski C. J., Brogan C. L., Hunter T. R., Churchwell E., 2009, *ApJ*, 702, 1615. doi:10.1088/0004-637X/702/2/1615
- de Wit W. J., Testi L., Palla F., Zinnecker H., 2005, *A&A*, 437, 247. doi:10.1051/0004-6361:20042489
- Davies B., Hoare M. G., Lumsden S. L., Hosokawa T., Oudmaijer R. D., Urquhart J. S., Mottram J. C., et al., 2011, *MNRAS*, 416, 972. doi:10.1111/j.1365-2966.2011.19095.x
- Dirienzo W. J., Brogan C., Indebetouw R., Chandler C. J., Friesen R. K., Devine K. E., 2015, *AJ*, 150, 159. doi:10.1088/0004-6256/150/5/159
- Dunne L., Eales S., Ivison R., Morgan H., Edmunds M., 2003, *Natur*, 424, 285. doi:10.1038/nature01792
- Egan M. P., Shipman R. F., Price S. D., Carey S. J., Clark F. O., Cohen M., 1998, *ApJL*, 494, L199. doi:10.1086/311198
- Elia D., Molinari S., Schisano E., Pestalozzi M., Pezzuto S., Merello M., Noriega-Crespo A., et al., 2017, *MNRAS*, 471, 100. doi:10.1093/mnras/stx1357
- Faúndez S., Bronfman L., Garay G., Chini R., Nyman L.-A., May J., 2004, *A&A*, 426, 97. doi:10.1051/0004-6361:20035755
- Furuya R. S., Cesaroni R., Shinnaga H., 2011, *A&A*, 525, A72. doi:10.1051/0004-6361/201014402
- Garay G., Lizano S., 1999, *PASP*, 111, 1049. doi:10.1086/316416
- Giannetti A., Leurini S., Wyrowski F., Urquhart J., Csengeri T., Menten K. M., König C., et al., 2017, *A&A*, 603, A33. doi:10.1051/0004-6361/201630048
- Guzmán A. E., Sanhueza P., Contreras Y., Smith H. A., Jackson J. M., Hoq S., Rathborne J. M., 2015, *ApJ*, 815, 130. doi:10.1088/0004-637X/815/2/130
- Hernández-Hernández V., Zapata L., Kurtz S., Garay G., 2014, *ApJ*, 786, 38. doi:10.1088/0004-637X/786/1/38
- Hoare M. G., Purcell C. R., Churchwell E. B., Diamond P., Cotton W. D., Chandler C. J., Smethurst S., et al., 2012, *PASP*, 124, 939. doi:10.1086/668058
- Hoare M. G., Kurtz S. E., Lizano S., Keto E., Hofner P., 2007, *prpl.conf*, 181
- Hosokawa T., Omukai K., 2009, *ApJ*, 691, 823. doi:10.1088/0004-637X/691/1/823
- Hsu S.-Y., Liu S.-Y., Liu T., Sahu D., Hirano N., Lee C.-F., Tatematsu K., et al., 2020, *ApJ*, 898, 107. doi:10.3847/1538-4357/ab9f3a
- Jiménez-Serra I., Vasyunin A. I., Caselli P., Marcelino N., Billot N., Viti S., Testi L., et al., 2016, *ApJL*, 830, L6. doi:10.3847/2041-8205/830/1/L6
- Jorgensen J. K., Belloche A., Garrod R. T., 2020, *arXiv*, arXiv:2006.07071
- Kennicutt R. C., 2005, *IAUS*, 227, 3. doi:10.1017/S1743921305004308
- Keto E., Zhang Q., 2010, *MNRAS*, 406, 102. doi:10.1111/j.1365-2966.2010.16672.x
- Keto E., 2007, *ApJ*, 666, 976. doi:10.1086/520320
- Keto E., Zhang Q., Kurtz S., 2008, *ApJ*, 672, 423. doi:10.1086/522570
- Krumholz M. R., McKee C. F., 2008, *Natur*, 451, 1082. doi:10.1038/nature06620
- Kurtz S., Hofner P., 2005, *AJ*, 130, 711. doi:10.1086/431546
- Kurtz S., Cesaroni R., Churchwell E., Hofner P., Walmsley C. M., 2000, *prpl.conf*, 299
- Kurtz S., Churchwell E., Wood D. O. S., 1994, *ApJS*, 91, 659. doi:10.1086/191952
- Ladeyschikov D. A., Bayandina O. S., Sobolev A. M., 2019, *AJ*, 158, 233. doi:10.3847/1538-3881/ab4b4c
- Li S., Zhang Q., Pillai T., Stephens I. W., Wang J., Li F., 2019, *ApJ*, 886, 130. doi:10.3847/1538-4357/ab464e
- Li S., Zhang Q., Liu H. B., Beuther H., Palau A., Girart J. M., Smith H., et al., 2020, *ApJ*, 896, 110. doi:10.3847/1538-4357/ab84f1
- Liu T., Kim K.-T., Yoo H., Liu S.-Y., Tatematsu K., Qin S.-L., Zhang Q., et al., 2016, *ApJ*, 829, 59. doi:10.3847/0004-637X/829/2/59
- Liu T., Lacy J., Li P. S., Wang K., Qin S.-L., Zhang Q., Kim K.-T., et al., 2017, *ApJ*, 849, 25. doi:10.3847/1538-4357/aa8d73
- Liu T., Evans N. J., Kim K.-T., Goldsmith P. F., Liu S.-Y., Zhang Q., Tatematsu K., et al., 2020a, *MNRAS*, 496, 2790. doi:10.1093/mnras/staa1577
- Liu T., Evans N. J., Kim K.-T., Goldsmith P. F., Liu S.-Y., Zhang Q., Tatematsu K., et al., 2020b, *MNRAS*, 496, 2821. doi:10.1093/mnras/staa1501
- McKee C. F., Tan J. C., 2003, *ApJ*, 585, 850. doi:10.1086/346149
- McMullin J. P., Waters B., Schiebel D., Young W., Golap K., 2007, *ASPC*, 376, 127
- Molet J., Brouillet N., Nony T., Gusdorf A., Motte F., Despois D., Louvet F., et al., 2019, *A&A*, 626, A132. doi:10.1051/0004-6361/201935497
- Motte F., Bontemps S., Louvet F., 2018, *ARA&A*, 56, 41. doi:10.1146/annurev-astro-091916-055235
- Nguyen-Luong Q., Anderson L. D., Motte F., Kim K.-T., Schilke P., Carloff P., Beuther H., et al., 2017, *ApJL*, 844, L25. doi:10.3847/2041-8213/aa7d48
- Osorio M., Lizano S., D'Alessio P., 1999, *ApJ*, 525, 808. doi:10.1086/307929
- Ossenkopf V., Henning T., 1994, *A&A*, 291, 943
- Osterbrock D. E., Ferland G. J., 2006, *agna.book*
- Perault M., Omont A., Simon G., Seguin P., Ojha D., Blommaert J., Felli M., et al., 1996, *A&A*, 315, L165
- Peretto N., Fuller G. A., 2009, *A&A*, 505, 405. doi:10.1051/0004-6361/200912127
- Pollack J. B., Hollenbach D., Beckwith S., Simonelli D. P., Roush T., Fong W., 1994, *ApJ*, 421, 615. doi:10.1086/173677
- Purcell C. R., Longmore S. N., Burton M. G., Walsh A. J., Minier V., Cunningham M. R., Balasubramanyam R., 2009, *MNRAS*, 394, 323. doi:10.1111/j.1365-2966.2008.14283.x
- Purcell C. R., Hoare M. G., Cotton W. D., Lumsden S. L., Urquhart J. S., Chandler C., Churchwell E. B., et al., 2013, *ApJS*, 205, 1. doi:10.1088/0067-0049/205/1/1
- Qin S.-L., Huang M., Wu Y., Xue R., Chen S., 2008, *ApJL*, 686, L21. doi:10.1086/592785
- Qin S.-L., Schilke P., Wu J., Wu Y., Liu T., Liu Y., Sánchez-Monge Á., 2015, *ApJ*, 803, 39. doi:10.1088/0004-637X/803/1/39
- Qiu K., Zhang Q., Beuther H., Fallscheer C., 2012, *ApJ*, 756, 170. doi:10.1088/0004-637X/756/2/170
- Ragan S. E., Bergin E. A., Plume R., Gibson D. L., Wilner D. J., O'Brien S., Hails E., 2006, *ApJS*, 166, 567. doi:10.1086/506594
- Rathborne J. M., Jackson J. M., Chambers E. T., Simon R., Shipman R., Frieswijk W., 2005, *ApJL*, 630, L181. doi:10.1086/491656
- Rathborne J. M., Jackson J. M., Chambers E. T., Stojimirovic I., Simon R., Shipman R., Frieswijk W., 2010, *ApJ*, 715, 310. doi:10.1088/0004-637X/715/1/310
- Rathborne J. M., Garay G., Jackson J. M., Longmore S., Zhang Q., Simon R., 2011, *ApJ*, 741, 120. doi:10.1088/0004-637X/741/2/120
- Rathborne J. M., Jackson J. M., Simon R., 2006, *ApJ*, 641, 389. doi:10.1086/500423
- Reid M. J., Menten K. M., Brunthaler A., Zheng X. W., Dame T. M., Xu Y., Wu Y., et al., 2014, *ApJ*, 783, 130. doi:10.1088/0004-637X/783/2/130
- Reid M. J., Menten K. M., Brunthaler A., Zheng X. W., Dame T. M., Xu Y., Li J., et al., 2019, *ApJ*, 885, 131. doi:10.3847/1538-4357/ab4a11
- Rivera-Soto R., Galván-Madrid R., Ginsburg A., Kurtz S., 2020, *ApJ*, 899, 94. doi:10.3847/1538-4357/aba749

Rosolowsky E. W., Pineda J. E., Kauffmann J., Goodman A. A., 2008, *ApJ*, 679, 1338. doi:10.1086/587685

Sánchez-Monge Á., Schilke P., Schmiedeke A., Ginsburg A., Cesaroni R., Lis D. C., Qin S.-L., et al., 2017, *A&A*, 604, A6. doi:10.1051/0004-6361/201730426

Sanhueza P., Contreras Y., Wu B., Jackson J. M., Guzmán A. E., Zhang Q., Li S., et al., 2019, *ApJ*, 886, 102. doi:10.3847/1538-4357/ab45e9

Sato K., Hasegawa T., Umemoto T., Saito H., Kuno N., Seta M., Sakamoto S., 2020, *arXiv*, arXiv:2006.13191

Schuller F., Menten K. M., Contreras Y., Wyrowski F., Schilke P., Bronfman L., Henning T., et al., 2009, *A&A*, 504, 415. doi:10.1051/0004-6361/200811568

Silva A., Zhang Q., Sanhueza P., Lu X., Beltrán M. T., Fallscheer C., Beuther H., et al., 2017, *ApJ*, 847, 87. doi:10.3847/1538-4357/aa88c6

Simon R., Jackson J. M., Rathborne J. M., Chambers E. T., 2006, *ApJ*, 639, 227. doi:10.1086/499342

Sollins P. K., Zhang Q., Keto E., Ho P. T. P., 2005, *ApJL*, 624, L49. doi:10.1086/430270

Soma T., Sakai N., Watanabe Y., Yamamoto S., 2018, *ApJ*, 854, 116. doi:10.3847/1538-4357/aaa70c

Svoboda B. E., Shirley Y. L., Traficante A., Battersby C., Fuller G. A., Zhang Q., Beuther H., et al., 2019, *ApJ*, 886, 36. doi:10.3847/1538-4357/ab40ca

Tan J. C., Beltrán M. T., Caselli P., Fontani F., Fuente A., Krumholz M. R., McKee C. F., et al., 2014, *prpl.conf*, 149. doi:10.2458/azu_uapress_9780816531240-ch007

Urquhart J. S., Moore T. J. T., Csengeri T., Wyrowski F., Schuller F., Hoare M. G., Lumsden S. L., et al., 2014, *MNRAS*, 443, 1555. doi:10.1093/mnras/stu1207

Urquhart J. S., Thompson M. A., Moore T. J. T., Purcell C. R., Hoare M. G., Schuller F., Wyrowski F., et al., 2013, *MNRAS*, 435, 400. doi:10.1093/mnras/stt1310

Urquhart J. S., König C., Giannetti A., Leurini S., Moore T. J. T., Eden D. J., Pillai T., et al., 2018, *MNRAS*, 473, 1059. doi:10.1093/mnras/stx2258

van der Tak F. F. S., 2004, *IAUS*, 221, 59

Vastel C., Ceccarelli C., Lefloch B., Bachiller R., 2014, *ApJL*, 795, L2. doi:10.1088/2041-8205/795/1/L2

Wang K., Zhang Q., Wu Y., Zhang H., 2011, *ApJ*, 735, 64. doi:10.1088/0004-637X/735/1/64

Wang K., Zhang Q., Testi L., van der Tak F., Wu Y., Zhang H., Pillai T., et al., 2014, *MNRAS*, 439, 3275. doi:10.1093/mnras/stu127

Wenger T. V., Balser D. S., Anderson L. D., Bania T. M., 2018, *ApJ*, 856, 52. doi:10.3847/1538-4357/aaec8

Wood D. O. S., Churchwell E., 1989, *ApJS*, 69, 831. doi:10.1086/191329

Xu J.-L., Wang J.-J., 2013, *MNRAS*, 431, 2385. doi:10.1093/mnras/stt331

Yang A. Y., Thompson M. A., Tian W. W., Bihr S., Beuther H., Hindson L., 2019, *MNRAS*, 482, 2681. doi:10.1093/mnras/sty2811

Yang A., Urquhart J., Thompson M., Menten K., Wyrowski F., Brunthaler A., Tian W., et al., 2020, *arXiv*, arXiv:2011.07620

Yuan J., Wu Y., Ellingsen S. P., Evans N. J., Henkel C., Wang K., Liu H.-L., et al., 2017, *ApJS*, 231, 11. doi:10.3847/1538-4365/aa7204

Young C. H., Evans N. J., 2005, *ApJ*, 627, 293. doi:10.1086/430436

Zinnecker H., Yorke H. W., 2007, *ARA&A*, 45, 481. doi:10.1146/annurev.astro.44.051905.092549

Zhang Q., Wang Y., Pillai T., Rathborne J., 2009, *ApJ*, 696, 268. doi:10.1088/0004-637X/696/1/268

Zhang Q., Wang K., Lu X., Jiménez-Serra I., 2015, *ApJ*, 804, 141. doi:10.1088/0004-637X/804/2/141

Zhang Q., Hunter T. R., Brand J., Sridharan T. K., Molinari S., Kramer M. A., Cesaroni R., 2001, *ApJL*, 552, L167. doi:10.1086/320345

Zhang Q., Hunter T. R., Brand J., Sridharan T. K., Cesaroni R., Molinari S., Wang J., et al., 2005, *ApJ*, 625, 864. doi:10.1086/429660

APPENDIX A: CALCULATION OF DISTANCES

Due to the lack of distance uncertainty information from the literature (Faúndez et al. 2004; Urquhart et al. 2018) for the 146 target

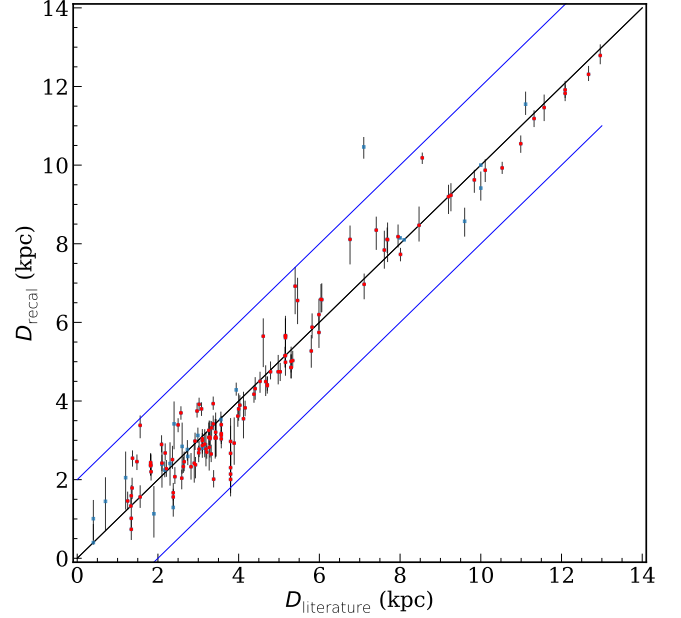


Figure A1. Comparison between the distances calculated in this work and those from the literature for the 146 ATOMS clumps. The black and blue lines indicate unity and 2.0 kpc offsets, respectively.

clumps, their kinematic distances were recalculated using the Monte Carlo kinematic distance tool developed by Wenger et al. (2018). With the Galactic coordinates and radial velocity parameters of a source inputted, the tool can return the distances and the uncertainties for the source leveraging the rotation curve of Reid et al. (2014) with the updated solar motion parameters (Reid et al. 2019) and the Monte Carlo technique with 10,000 samplings. The radial velocity measurements by Liu et al. (2016) rather than by Bronfman, Nyman, & May (1996) were adopted in this work since the velocity resolution (0.42 km s^{-1}) in Liu et al. (2016) at which the measurements were made better than that (0.76 km s^{-1}) in Bronfman, Nyman, & May (1996).

Apart from the two sources located near the Galactic center, kinematic distance solutions have been calculated for 144 ATOMS clumps. The distance ambiguities (if any) have been resolved following Faúndez et al. (2004); Urquhart et al. (2018). Moreover, the kinematic distance solutions have been improved for the three sources using maser parallax distances available in the literature (Reid et al. 2014; Urquhart et al. 2018). Overall, the typical relative distance uncertainty for the 144 ATOMS clumps is $\sim 7\%$. For the remaining two sources located near the Galactic center, their kinematic distances could not be calculated from the rotation curve and thus the values from the literature along with a typical relative distance uncertainty of $\sim 7\%$ have been adopted. The recalculated distances are listed in Table A.

Comparing the recalculated distances with those from Faúndez et al. (2004); Urquhart et al. (2018), we find a good agreement (Pearson correlation coefficient ρ is 0.97) as shown in Fig. A1. In addition, the relative distance uncertainties are found to have an IQR of $\sim [5\%, 12\%]$ with a median value of $\sim 7\%$.

Table A1. Distances of 146 ATOMS clumps.

ID	Name	l deg	b deg	V_{lsr} km s ⁻¹	D kpc	ID	Name	l deg	b deg	V_{lsr} km s ⁻¹	D kpc
1	I08076-3556	253.2952	-1.6159	5.9 ± 0.4	1.0 ^{+0.5} _{-0.5}	74	I16385-4619	338.5690	-0.1441	-117.8 ± 0.4	7.0 ^{+0.3} _{-0.4}
2	I08303-4303	261.6457	-2.0911	15.2 ± 0.4	2.4 ^{+0.5} _{-0.6}	75	I16424-4531	339.6226	-0.1225	-31.1 ± 0.4	2.3 ^{+0.3} _{-0.2}
3	I08448-4343	263.7731	-0.4337	3.4 ± 0.4	1.4 ^{+0.6} _{-0.8}	76	I16445-4459	340.2492	-0.0458	-121.4 ± 0.4	8.2 ^{+0.3} _{-0.2}
4	I08470-4243	263.2493	0.5114	13.5 ± 0.4	2.4 ^{+0.6} _{-0.7}	77	I16458-4512	340.2475	-0.3741	-49.9 ± 0.4	3.5 ^{+0.2} _{-0.2}
5	I09002-4732	268.4203	-0.8476	3.9 ± 0.4	2.0 ^{+0.7} _{-0.8}	78	I16484-4603	339.8842	-1.2572	-31.6 ± 0.4	2.4 ^{+0.2} _{-0.2}
6	I09018-4816	269.1529	-1.1308	10.8 ± 0.4	2.8 ^{+0.6} _{-0.7}	79	I16487-4423	341.2158	-0.2358	-43.2 ± 0.4	3.3 ^{+0.2} _{-0.2}
7	I09094-4803	269.8498	-0.0633	74.6 ± 0.5	8.6 ^{+0.3} _{-0.4}	80	I16489-4431	341.1258	-0.3475	-40.4 ± 0.4	3.1 ^{+0.2} _{-0.2}
8	I10365-5803	286.2076	0.1708	-18.9 ± 0.4	3.4 ^{+0.6} _{-0.6}	81	I16506-4512	340.7842	-1.0157	-25.8 ± 0.4	2.1 ^{+0.2} _{-0.2}
9	I11298-6155	293.8275	-0.7457	33.0 ± 0.4	9.4 ^{+0.4} _{-0.3}	82	I16524-4300	342.7076	0.1258	-40.6 ± 0.4	3.2 ^{+0.2} _{-0.2}
10	I11332-6258	294.5109	-1.6218	-16.1 ± 0.5	1.1 ^{+0.7} _{-0.6}	83	I16547-4247	343.1275	-0.0625	-29.7 ± 0.4	2.6 ^{+0.2} _{-0.2}
11	I11590-6452	297.7209	-2.7820	-3.9 ± 0.4	0.4 ^{+0.5} _{-0.1}	84	I16562-3959	345.4926	1.4686	-11.9 ± 0.4	1.3 ^{+0.2} _{-0.2}
12	I12320-6122	300.9692	1.1456	-42.5 ± 0.4	3.1 ^{+0.6} _{-0.5}	85	I16571-4029	345.1927	1.0288	-14.7 ± 0.4	1.6 ^{+0.2} _{-0.2}
13	I12326-6245	301.1358	-0.2258	-39.1 ± 0.4	5.6 ^{+0.5} _{-0.8}	86	I17006-4215	344.2208	-0.5941	-24.2 ± 0.4	2.3 ^{+0.2} _{-0.2}
14	I12383-6128	301.7308	1.1040	-37.9 ± 0.4	2.8 ^{+0.7} _{-0.6}	87	I17008-4040	345.5043	0.3475	-15.9 ± 0.4	1.7 ^{+0.2} _{-0.2}
15	I12572-6316	303.9308	-0.6874	29.5 ± 0.4	11.5 ^{+0.3} _{-0.3}	88	I17016-4124	345.0029	-0.2241	-26.5 ± 0.4	2.5 ^{+0.2} _{-0.2}
16	I13079-6218	305.2091	0.2058	-40.5 ± 0.4	3.0 ^{+0.6} _{-0.7}	89	I17136-3617	350.5074	0.9590	-10.3 ± 0.4	1.6 ^{+0.3} _{-0.2}
17	I13080-6229	305.1958	0.0342	-34.0 ± 0.4	2.3 ^{+0.6} _{-0.6}	90	I17143-3700	350.0158	0.4325	-31.3 ± 0.4	12.3 ^{+0.2} _{-0.2}
18	I13111-6228	305.5624	0.0142	-38.7 ± 0.4	2.7 ^{+0.7} _{-0.6}	91	I17158-3901	348.5492	-0.9789	-15.8 ± 0.4	2.0 ^{+0.2} _{-0.2}
19	I13134-6242	305.7989	-0.2441	-31.6 ± 0.4	2.0 ^{+0.6} _{-0.4}	92	I17160-3707	350.1025	0.0825	-69.7 ± 0.4	9.9 ^{+0.2} _{-0.2}
20	I13140-6226	305.8872	0.0158	-32.7 ± 0.4	2.1 ^{+0.6} _{-0.5}	93	I17175-3544	351.4159	0.6457	-5.7 ± 0.4	1.0 ^{+0.3} _{-0.3}
21	I13291-6229	307.6158	-0.2592	-37.1 ± 0.4	2.4 ^{+0.6} _{-0.5}	94	I17204-3636	351.0411	-0.3357	-17.8 ± 0.4	2.7 ^{+0.2} _{-0.2}
22	I13291-6249	307.5608	-0.5875	-32.4 ± 0.4	7.8 ^{+0.5} _{-0.5}	95	I17220-3609	351.5809	-0.3524	-95.0 ± 0.4	7.7 ^{+0.2} _{-0.2}
23	I13295-6152	307.7558	0.3525	-43.5 ± 0.5	2.9 ^{+0.7} _{-0.6}	96	I17233-3606	351.7742	-0.5374	-4.2 ± 0.4	0.7 ^{+0.3} _{-0.3}
24	I13471-6120	309.9208	0.4775	-57.3 ± 0.4	6.6 ^{+0.6} _{-0.6}	97	I17244-3536	352.3158	-0.4425	-9.4 ± 0.4	1.8 ^{+0.3} _{-0.3}
25	I13484-6100	310.1442	0.7591	-54.1 ± 0.4	6.9 ^{+0.5} _{-0.7}	98	I17258-3637	351.6326	-1.2538	-11.7 ± 0.4	2.0 ^{+0.2} _{-0.3}
26	I14013-6105	311.6257	0.2891	-54.6 ± 0.4	3.5 ^{+0.7} _{-0.5}	99	I17269-3312	354.5959	0.4691	-20.7 ± 0.5	4.2 ^{+0.2} _{-0.2}
27	I14050-6056	312.1078	0.3091	-48.1 ± 0.4	3.1 ^{+0.5} _{-0.5}	100	I17271-3439	353.4091	-0.3607	-15.9 ± 0.6	3.0 ^{+0.2} _{-0.2}
28	I14164-6028	313.5758	0.3242	-45.2 ± 0.4	2.8 ^{+0.4} _{-0.4}	101	I17278-3541	352.6308	-1.0674	0.7 ± 0.4	1.3 ^{+0.2} _{-0.0}
29	I14206-6151	313.5758	-1.1540	-48.8 ± 0.4	3.0 ^{+0.5} _{-0.5}	102	I17439-2845	0.3160	-0.2008	18.8 ± 0.4	8.1 ^{+0.0} _{-0.0}
30	I14212-6131	313.7658	-0.8624	-49.2 ± 0.4	3.1 ^{+0.5} _{-0.5}	103	I17441-2822	0.6659	-0.0341	51.5 ± 1.6	8.1 ^{+0.6} _{-0.6}
31	I14382-6017	316.1392	-0.5058	-60.3 ± 0.4	8.1 ^{+0.4} _{-0.6}	104	I17455-2800	1.1258	-0.1075	-14.2 ± 0.4	10.0 ^{+0.7} _{-0.7}
32	I14453-5912	317.4074	0.1092	-40.2 ± 0.4	2.3 ^{+0.3} _{-0.3}	105	I17545-2357	5.6374	0.2375	9.2 ± 0.4	2.4 ^{+0.2} _{-0.3}
33	I14498-5856	318.0495	0.0858	-49.7 ± 0.4	2.9 ^{+0.4} _{-0.3}	106	I17589-2312	6.7959	-0.2575	21.6 ± 0.5	3.7 ^{+0.2} _{-0.2}
34	I15122-5801	321.0545	-0.5073	-60.3 ± 0.4	9.2 ^{+0.3} _{-0.4}	107	I17599-2148	8.1408	0.2225	19.8 ± 0.4	3.1 ^{+0.2} _{-0.2}
35	I15254-5621	323.4591	-0.0791	-66.9 ± 0.4	3.8 ^{+0.4} _{-0.3}	108	I18032-2032	9.6209	0.1942	5.9 ± 0.4	5.2 ^{+0.2} _{-0.3}
36	I15290-5546	324.2011	0.1208	-88.5 ± 0.4	8.1 ^{+0.4} _{-0.6}	109	I18056-1952	10.4725	0.0275	66.7 ± 0.4	10.2 ^{+0.1} _{-0.2}
37	I15384-5348	326.4457	0.9073	-40.6 ± 0.4	2.4 ^{+0.3} _{-0.3}	110	I18075-2040	10.0008	-0.7541	31.5 ± 0.4	3.8 ^{+0.2} _{-0.2}
38	I15394-5358	326.4741	0.7024	-40.7 ± 0.4	2.4 ^{+0.3} _{-0.2}	111	I18079-1756	12.4176	0.5058	18.4 ± 0.4	2.2 ^{+0.2} _{-0.2}
39	I15408-5356	326.6573	0.5940	-40.1 ± 0.4	2.4 ^{+0.3} _{-0.3}	112	I18089-1732	12.8875	0.4891	33.5 ± 0.4	3.4 ^{+0.2} _{-0.2}
40	I15411-5352	326.7240	0.6140	-41.0 ± 0.4	2.4 ^{+0.2} _{-0.3}	113	I18110-1854	11.9355	-0.6156	39.0 ± 0.4	3.9 ^{+0.2} _{-0.2}
41	I15437-5343	327.1194	0.5090	-83.8 ± 0.5	4.7 ^{+0.4} _{-0.3}	114	I18116-1646	13.8725	0.2808	50.2 ± 0.4	4.3 ^{+0.2} _{-0.2}
42	I15439-5449	326.4724	-0.3774	-53.4 ± 0.4	3.1 ^{+0.3} _{-0.3}	115	I18117-1753	12.9075	-0.2591	38.0 ± 0.4	3.7 ^{+0.2} _{-0.2}
43	I15502-5302	328.3075	0.4309	-91.6 ± 0.4	5.3 ^{+0.4} _{-0.4}	116	I18134-1942	11.4974	-1.4853	10.7 ± 0.4	1.5 ^{+0.2} _{-0.2}
44	I15520-5234	328.8092	0.6325	-41.2 ± 0.4	2.5 ^{+0.3} _{-0.2}	117	I18139-1842	12.4310	-1.1138	40.0 ± 0.4	3.9 ^{+0.2} _{-0.2}
45	I15522-5411	327.8092	-0.6358	-46.8 ± 0.4	2.8 ^{+0.2} _{-0.3}	118	I18159-1648	14.3308	-0.6440	23.9 ± 0.4	2.5 ^{+0.2} _{-0.2}
46	I15557-5215	329.4691	0.5024	-67.6 ± 0.4	3.9 ^{+0.3} _{-0.3}	119	I18182-1433	16.5858	-0.0508	60.1 ± 0.4	4.4 ^{+0.2} _{-0.2}
47	I15567-5236	329.3374	0.1475	-107.3 ± 0.4	6.2 ^{+0.4} _{-0.4}	120	I18223-1243	18.6542	-0.0591	46.0 ± 0.4	3.4 ^{+0.2} _{-0.2}
48	I15570-5227	329.4724	0.2158	-100.2 ± 0.4	5.7 ^{+0.5} _{-0.4}	121	I18228-1312	18.3010	-0.3891	33.6 ± 0.4	2.7 ^{+0.2} _{-0.2}
49	I15584-5247	329.4241	-0.1624	-76.2 ± 0.4	4.3 ^{+0.4} _{-0.3}	122	I18236-1205	19.3625	-0.0308	27.8 ± 0.4	2.2 ^{+0.2} _{-0.2}
50	I15596-5301	329.4058	-0.4591	-73.9 ± 0.4	9.9 ^{+0.3} _{-0.3}	123	I18264-1152	19.8825	-0.5341	45.4 ± 0.4	3.3 ^{+0.2} _{-0.2}

APPENDIX B: CALCULATION OF MASS AND MASS SURFACE DENSITY

To understand the nature of the 90 COM-containing cores not associated the H/UC-HII signature (see Sect. 3.2.2) and 274 “unknown”

cores, we calculated their mass M_{core} in the following form:

$$M_{\text{core}} = \frac{F_{\nu}^{\text{int}} R_{\text{gd}} D^2}{B_{\nu}(T_{\text{dust}}) \kappa_{\nu}}, \quad (\text{B1})$$

where F_{ν}^{int} is the measured integrated 3 mm flux over the core size, R_{gd} is the gas-to-dust mass ratio (assumed to be 100), D is the

Table A1 – continued Distances of 146 ATOMS clumps.

ID	Name	l deg	b deg	V_{lsr} km s ⁻¹	D kpc	ID	Name	l deg	b deg	V_{lsr} km s ⁻¹	D kpc
51	I16026-5035	331.3608	1.0657	-78.5 ± 0.4	4.5 ^{+0.2} _{-0.3}	124	I18290-0924	22.3508	0.0675	84.3 ± 0.4	5.0 ^{+0.2} _{-0.2}
52	I16037-5223	330.2943	-0.3941	-81.0 ± 0.4	9.6 ^{+0.3} _{-0.3}	125	I18308-0503	26.4212	1.6902	43.6 ± 0.4	2.8 ^{+0.2} _{-0.2}
53	I16060-5146	330.9542	-0.1825	-88.8 ± 0.4	5.0 ^{+0.4} _{-0.3}	126	I18311-0809	23.7107	0.1708	113.5 ± 0.4	6.6 ^{+0.4} _{-0.3}
54	I16065-5158	330.8792	-0.3675	-61.5 ± 0.4	3.6 ^{+0.3} _{-0.3}	127	I18314-0720	24.4709	0.4874	102.1 ± 0.5	5.9 ^{+0.2} _{-0.3}
55	I16071-5142	331.1325	-0.2442	-85.9 ± 0.5	4.9 ^{+0.3} _{-0.3}	128	I18316-0602	25.6492	1.0507	45.3 ± 0.4	2.9 ^{+0.2} _{-0.2}
56	I16076-5134	331.2792	-0.1891	-86.0 ± 0.4	4.9 ^{+0.3} _{-0.3}	129	I18317-0513	26.3808	1.4071	42.2 ± 0.4	2.7 ^{+0.2} _{-0.2}
57	I16119-5048	332.2958	-0.0941	-48.4 ± 0.4	3.0 ^{+0.2} _{-0.3}	130	I18317-0757	23.9539	0.1508	80.5 ± 0.4	4.7 ^{+0.3} _{-0.2}
58	I16132-5039	332.5440	-0.1241	-47.0 ± 0.4	2.9 ^{+0.3} _{-0.2}	131	I18341-0727	24.6725	-0.1508	113.5 ± 0.4	6.6 ^{+0.4} _{-0.3}
59	I16158-5055	332.6474	-0.6090	-49.4 ± 0.4	3.0 ^{+0.2} _{-0.2}	132	I18411-0338	28.8608	0.0659	103.7 ± 0.4	8.3 ^{+0.3} _{-0.5}
60	I16164-5046	332.8256	-0.5490	-56.2 ± 0.4	3.4 ^{+0.2} _{-0.2}	133	I18434-0242	29.9538	-0.0158	98.1 ± 0.4	5.7 ^{+0.4} _{-0.4}
61	I16172-5028	333.1344	-0.4307	-52.1 ± 0.4	3.2 ^{+0.2} _{-0.2}	134	I18440-0148	30.8175	0.2742	98.3 ± 0.4	5.7 ^{+0.5} _{-0.3}
62	I16177-5018	333.3077	-0.3657	-50.9 ± 0.4	3.1 ^{+0.2} _{-0.2}	135	I18445-0222	30.3860	-0.1041	87.2 ± 0.4	5.0 ^{+0.3} _{-0.3}
63	I16272-4837	335.5857	-0.2908	-45.8 ± 0.4	3.0 ^{+0.2} _{-0.2}	136	I18461-0113	31.5808	0.0775	97.1 ± 0.4	5.6 ^{+0.4} _{-0.5}
64	I16297-4757	336.3593	-0.1374	-79.9 ± 0.4	4.7 ^{+0.2} _{-0.2}	137	I18469-0132	31.3958	-0.2575	86.9 ± 0.4	5.2 ^{+0.4} _{-0.3}
65	I16304-4710	337.0042	0.3225	-61.0 ± 0.4	11.2 ^{+0.2} _{-0.2}	138	I18479-0005	32.7973	0.1908	15.1 ± 0.4	12.8 ^{+0.3} _{-0.2}
66	I16313-4729	336.8658	0.0042	-72.3 ± 0.4	4.4 ^{+0.2} _{-0.2}	139	I18502+0051	34.2601	-0.4259	53.0 ± 0.4	10.5 ^{+0.3} _{-0.3}
67	I16318-4724	336.9942	-0.0275	-120.5 ± 0.4	8.1 ^{+0.3} _{-0.3}	140	I18507+0110	34.2575	0.1542	58.5 ± 0.4	1.6 ^{+0.3} _{-0.3}
68	I16330-4725	337.1208	-0.1741	-74.1 ± 0.4	10.5 ^{+0.2} _{-0.2}	141	I18507+0121	34.4108	0.2342	58.2 ± 0.4	3.4 ^{+0.3} _{-0.3}
69	I16344-4658	337.6125	-0.0592	-48.9 ± 0.4	11.8 ^{+0.2} _{-0.2}	142	I18517+0437	37.4308	1.5188	44.1 ± 0.4	2.5 ^{+0.4} _{-0.2}
70	I16348-4654	337.7042	-0.0541	-47.2 ± 0.4	11.9 ^{+0.2} _{-0.2}	143	I18530+0215	35.4657	0.1408	77.8 ± 0.4	4.5 ^{+0.4} _{-0.4}
71	I16351-4722	337.4058	-0.4025	-40.3 ± 0.4	2.8 ^{+0.2} _{-0.2}	144	I19078+0901	43.1658	0.0109	7.2 ± 0.4	11.5 ^{+0.3} _{-0.3}
72	I16362-4639	338.0642	-0.0675	-37.4 ± 0.4	2.7 ^{+0.2} _{-0.2}	145	I19095+0930	43.7941	-0.1275	44.7 ± 0.4	9.2 ^{+0.3} _{-0.4}
73	I16372-4545	338.8506	0.4091	-57.5 ± 0.4	3.8 ^{+0.2} _{-0.2}	146	I19097+0847	43.1791	-0.5191	57.3 ± 0.4	8.5 ^{+0.5} _{-0.4}

NOTE: I17441-2822 and 17455-2800 are close to the Galactic centre, whose distance values are adopted from Faúndez et al. (2004); I18469-0132, I18507+0110, and I19097+0847 have the maser parallax distance measurements (Reid et al. 2014).

distance to the core, B_ν is the Planck function for a dust temperature T_{dust} , and κ_ν is the opacity assumed to be $0.18 \text{ cm}^2 \text{ g}^{-1}$ of dust at $\nu \sim 94 \text{ GHz}$, taken directly from the “OH5” dust model, a combination of dust from Ossenkopf & Henning (1994) and Pollock et al. (1994) and extended to longer wavelengths by Young & Evans (2005). Moreover, the mass surface density Σ_{core} was derived from $\Sigma_{\text{core}} = M_{\text{core}}/(\pi R_{\text{core}}^2)$, where R_{core} is the core radius equal to the geometric mean of the $FWHM_{\text{maj}}^{\text{dec}}$, $FWHM_{\text{min}}^{\text{dec}}$ at the respective core distance. Given the median radius of the 90 COM-containing cores $\sim 0.02 \text{ pc}$, the $T_{\text{dust}} \sim 100 \text{ K}$ was assumed for a first-order approximation in the calculation, which is typical of HMCs at a radius of $\sim 0.01 \text{ pc}$ (Osorio, Lizano, & D’Alessio 1999). For the 274 “unknown” cores, the temperature 25 K is assumed, which is comparable to the mean value over the clumps that do not have cHMC or HUC-HII signatures.

The peak column densities are estimated from the peak flux density of the cores using the following equation:

$$N_{\text{H}_2} = \frac{F_\nu^p R_{\text{gd}}}{B_\nu(T_{\text{dust}}) \Omega \kappa_\nu \mu m_{\text{H}}}, \quad (\text{B2})$$

where Ω is the beam solid angle, μ is the mean molecular weight of the gas, assumed to be 2.8, m_{H} is the mass of the hydrogen atom. In turn, the number densities can be estimated via $n_{\text{H}_2} = N_{\text{H}_2}/2R$, assuming a spherical geometry for cores.

The three derived parameters M_{core} , n_{H_2} , and Σ_{core} are arranged in last three columns of Tables 2 for the 32 s-cHMCs, and of Table 3 for 58 w-cHMCs.

Author affiliations:

¹Department of Astronomy, Yunnan University, Kunming, 650091, PR China

²Shanghai Astronomical Observatory, Chinese Academy of Sciences, 80 Nandan Road, Shanghai 200030, Peoples Republic of China

³Key Laboratory for Research in Galaxies and Cosmology, Shanghai Astronomical Observatory, Chinese Academy of Sciences, 80 Nandan Road, Shanghai 200030, Peoples Republic of China

⁴Departamento de Astronomía, Universidad de Concepción, Av. Esteban Iturra s/n, Distrito Universitario, 160-C, Chile

⁵Department of Astronomy, The University of Texas at Austin, 2515 Speedway, Stop C1400, Austin, TX 78712-1205, USA

⁶Korea Astronomy and Space Science Institute, 776 Daedeokdaero, Yuseong-gu, Daejeon 34055, Republic of Korea

⁷Kavli Institute for Astronomy and Astrophysics, Peking University, 5 Yiheyuan Road, Haidian District, Beijing 100871, People’s Republic of China

⁸Departamento de Astronomía, Universidad de Chile, Las Condes, Santiago, Chile

⁹Max-Planck-Institute for Astronomy, Königstuhl 17, 69117 Heidelberg, Germany

¹⁰Jet Propulsion Laboratory, California Institute of Technology, 4800 Oak Grove Drive, Pasadena, CA 91109, USA

¹¹Institute of Astronomy and Astrophysics, Academia Sinica. 11F of Astronomy-Mathematics Building, AS/NTU No. 1, Section 4, Roosevelt Rd., Taipei 10617, Taiwan

¹²Indian Institute of Space Science and Technology, Thiruvananthapuram 695 547, Kerala, India

¹³Center for Astrophysics | Harvard & Smithsonian, 60 Garden Street, Cambridge, MA 02138, USA

¹⁴Department of Physics, P.O. Box 64, FI-00014, University of Helsinki, Finland

¹⁵National Astronomical Observatories, Chinese Academy of Sciences, Beijing 100101, China

¹⁶University of Chinese Academy of Sciences, Beijing 100049, China

¹⁷NAOC-UKZN Computational Astrophysics Centre, University of KwaZulu-Natal, Durban 4000, South Africa

¹⁸Key Laboratory of Radio Astronomy, Chinese Academy of Sciences, Nanjing 210008, People's Republic of China

¹⁹Department of Astronomy, Peking University, 100871, Beijing, People's Republic of China

²⁰University of Science and Technology, Korea (UST), 217 Gajeong-ro, Yuseong-gu, Daejeon 34113, Republic of Korea

²¹National Astronomical Observatory of Japan, National Institutes of Natural Sciences, 2-21-1 Osawa, Mitaka, Tokyo 181-8588, Japan

²²School of Physics, University of New South Wales, Sydney, NSW 2052, Australia

²³School of Space Research, Kyung Hee University, Yongin-Si, Gyeonggi-Do 17104, Republic of Korea

²⁴Astronomy Department, University of California, Berkeley, CA 94720, USA

²⁵IRAP, Université de Toulouse, CNRS, UPS, CNES, Toulouse, France

²⁶School of Physics and Astronomy, Sun Yat-sen University, 2 Daxue Road, Zhuhai, Guangdong, 519082, People's Republic of China

²⁷Eötvös Loránd University, Department of Astronomy, Pázmány Péter sétány 1/A, H-1117, Budapest, Hungary

²⁸College of Science, Yunnan Agricultural University, Kunming, 650201, People's Republic of China

²⁹Satyendra Nath Bose National Centre for Basic Sciences, Block-JD, Sector-III, Salt Lake, Kolkata-700 106

³⁰Physical Research Laboratory, Navrangpura, Ahmedabad 380 009, India

³¹Department of Physics, Taiyuan Normal University, Jinzhong 030619, China

³²SOFIA Science Centre, USRA, NASA Ames Research Centre, MS-12, N232, Moffett Field, CA 94035, USA